REDUCING MOTION INACCURACIES DUE TO COGGING IN A REDUNDANTLY ACTUATED 3-DOF MANIPULATOR

YINGYING LI
October, 2023

SUPERVISORS:

Dr.Ir.R.G.K.M. Aarts
Dr.J. Dasdemir

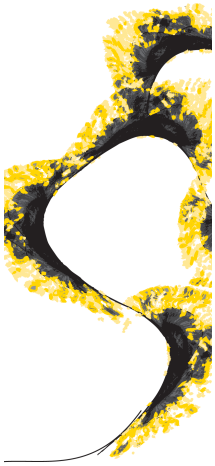

REDUCING MOTION INACCURACIES DUE TO COGGING IN A REDUNDANTLY ACTUATED 3-DOF MANIPULATOR

YINGYING LI

University of Twente, Enschede, The Netherlands
October, 2023

Specialization: MSc-Systems and control.
Chair of AMDA and PE

SUPERVISORS:

Dr.Ir.R.G.K.M. Aarts
Dr.J. Dasdemir

Examination committe:

Dr.Ir.R.G.K.M. Aarts (Chair)

Dr.J. Dasdemir
Dr.I.S.M.Khalil (External examiner)

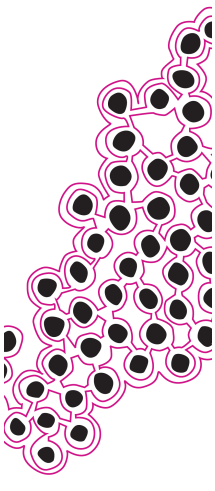

ABSTRACT

PKM are widely used in different fields owing to their advantages of high stiffness, low inertia, and high acceleration. In order to address the singularity problem of the parallel manipulator, RA-PKM has been developed. Previously, a 3DOF RA-PKM with compliant joints and redundant actuation was designed, constructed, and tested. However, the utilization of direct drive brushless actuators resulted in significant motion inaccuracies due to cogging behavior. Because of the magnetic attraction between the rotor's permanent magnet and the stator, cogging torque occurs. The cogging torque causes periodic variations that can lead to irregularities, hitches, or jerks in motion, ultimately impacting position control and performance accuracy.

This thesis focuses on developing a model to mitigate the cogging effect on the dynamic motion of the RA-PKM system. To start with, the kinematic and dynamic motion characteristics of the RA-PKM system have been thoroughly studied. Subsequently, the cogging torque data from the motors operating under diverse conditions were collected by a series of experiments. Based on the cogging torque data, the cogging torque equation was successfully derived by employing a parameter identification method. Meanwhile, the influence of the cogging torque on the dynamic motion of the manipulator was analyzed. In order to mitigate the cogging effect, two control methods, namely feedforward compensation method and feedback compensation method, were developed based on meticulous analyses as well as the application of control theory principles. The efficacy of both control methods was assessed through a combination of simulation and experimental studies, encompassing both single-arm system and the complete system. Here, the feedback control method demonstrated superior performance in enhancing the motion accuracy within the context of single-arm system. From the complete system, both methods appear no significant difference in improving the system performance. This is due to the inherent redundancy of the complete system.

Keywords

Compliant joints, Redundant actuation, Cogging torque, Motion accuracy

ACKNOWLEDGEMENTS

I am truly grateful for the tremendous support I received from Dr.Ir. Ronald Aarts during the entirety of my graduation project. Your extensive experience and profound theoretical knowledge are invaluable in assisting me with the completion of my thesis. Additionally, I would like to express my heartfelt appreciation to Dr.Janset Dasdemir for her invaluable contributions to the development of control algorithms. Her insightful ideas have greatly enriched my understanding of the thesis and research on the field. Lastly, I would like to extend my sincere thanks to all those who have been involved in my graduation project, without their support, this thesis could not be completed.

TABLE OF CONTENTS

List of Symbols

B_r	Fourier transformation coefficients of the flux density function
$\bar{C}$	Reduced Coriolis and centrifugal force
E	Magnetic field energy
F_e	External applied force on end-effector
$\mathscr{F}$	Geometric transfer function
$\mathbf{F}_{,q}$	First order of geometric transfer function
$\mathbf{F}_{,qq}$	Second order of geometric transfer function
f	Force/torque acting on the center of mass
G_n	Fourier transformation coefficients of the air gap function
$g(\theta)$	Basic function for fitting function
$H(q)$	Constraint equation
J	Jocabian matrix
M	Inertial matrix
m_{eq}	System equalized mass/intertia
$\bar{M}$	Reduced inertia matrix
L_s	Stack length
L_1	Length of upper arm
L_2	Length of lower arm
L_3	Length of inner square(End effector)
N_L	Least common multiple of the motor's stator slots and rotor poles
P	Parameters fitting function
O_f	Optimization objective function
q	Generalized coordinates for RA-PKM
q_d	Dependent coordinate
q_i	Independent coordinate
q_s	Generalized coordinate for forward kinematics
$\bar{Q}$	Stiffness torque
r	Distance from shoulder joint wrist joint
R_1, R_2	Stator bore radiu and magnet outer radius
$S(q)$	Constraint equation for forward kinematics
T_{cog}	Cogging torque
T_k	Amplitude of the k_{th} order for cogging simple equation
W	Weighting function
x	position x directon
y	position y direction
z	Number of stator slot
α	inner angle between shoulder arm and elbow arm
β	Angle between the line connecting the shoulder joint and the wrist joint and the shoulder arm.
$\epsilon_{,q}$	Relationship between shoulder angle and end effector position
θ	position rotation
λ	lagrange multiplier
μ_0	Air permeability
τ	Actuator torque
ϕ_k	The phase shift of the k_{th} order for cogging simple equation
ω_c	System crossover frequency

LIST OF FIGURES

LIST OF TABLES

Acronyms

AC alternating current. 2

BLDC Brushless direct current. 2, 3

DC direct current. 2

DOF Degree of freedom. 1, 3, 5

EE End effector. 1

EMF electromotive force. 3, 5

EOM Equation of motion. 11, 39

Finite Element Method Finite Element Method. 17

PID Proportional-Integral-Derivative control. 13

PKM Parallel kinematics manipulators. 1, 3, 5, 10

RA-PKM Redundanct actuator parallel kinematics manipulator. i, 1, 5, 7, 10, 43

RMSE Root mean square error. 26, 27, 35

Chapter 1

Introduction

1.1 PROBLEM STATEMENT

Parallel kinematics manipulators (PKM) are closed-loop kinematic systems in which the end effector (EE) is connected to multiple independent robotic arm systems. The PKM is widely used owing to its potential in system function such as high stiffness, speed, payload, and low inertia[1] ,[2]. However, there are also pitfalls which engineers are trying to improve, such as limited workspace and potential singularities. To address these issues meanwhile, to enhanced system precision, flexibility, as well as expand workspace, a redundant design for the actuators is widely proposed and used [3]. Redundanct actuator parallel kinematics manipulator (RA-PKM) design could not only enhance the reliability of the driving system as well as improve the system's load-carrying capacity and accelerating capabilities, but also could improve the safety and system reliability when one actuator breaks down[2]. Moreover, the design of redundant systems also enhances the overall rigidity of the robotic arm, resulting in improved motion accuracy[3].

In the previous graduation project, the manipulator with 3 DOF and redundant actuation has been designed, built, and tested, the structure can be seen in Figure 1.1. This 3-DOF RA-PKM include 4 shoulder elbow arms link with the wrist End effector (EE), the actuator is located at the shoulder point. More over, this RA-PKM is equipped with flexure joints, operating as a partially compliant mechanism [4]. The compliant mechanism is a monolithic system, this design implies that both the translational and rotational movements of the end-effector are achieved through the bending of the shoulder cartwheel flexure hinge, elbow and wrist butterfly flexure hinges as shown in Figure 1.2. In contrast to conventional rigid structures composed of interconnected rigid components, compliant mechanisms could not only transfer motion through joints but also harness the deformation of their flexible parts to generate motion[5],[6].

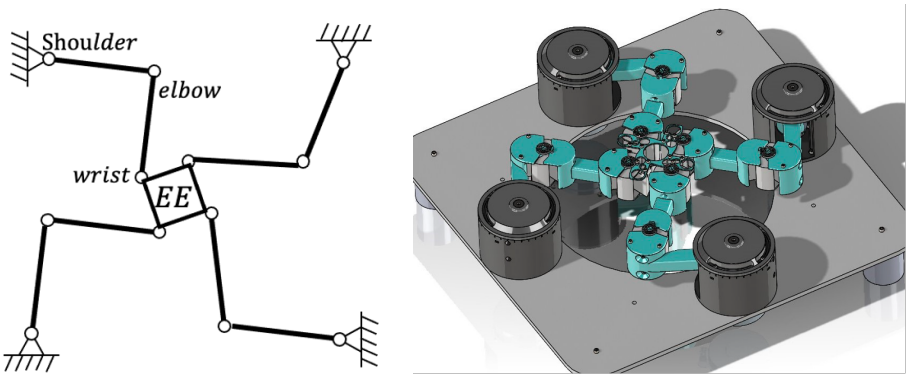

(a) Schematic of 3-DOF manipulator (b) 3-DOF manipulator CAD model

Figure 1.1: Schematic view of 3-DOF manipulator [7]

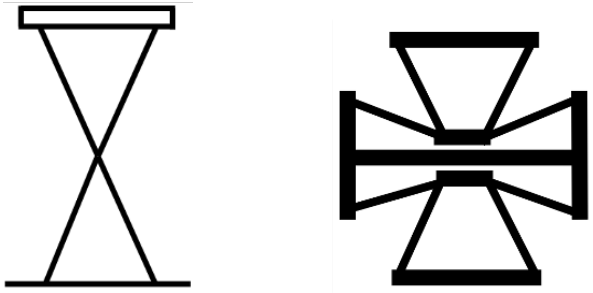

(a) Cartwheel flexure hinge

(b) Butterfly flexure hinge

Figure 1.2: Schematic view of flexure hinge [7]

The advantages of compliant mechanisms manifest predominantly in two key areas. Firstly, there's a reduction in overall costs. The streamlined design that entails fewer components, simplified assembly processes, and more straightforward manufacturing procedures could result in significant decrease of the overall cost. This simplicity not only translates into economic savings but also accelerates production timelines as well as reduces the potential human errors during assembly. Additionally, performance is substantially enhanced, encompassing enhanced precision, increased reliability, diminished wear and tear, reduced weight, and simplified maintenance. However, despite the numerous merits of flexible mechanisms, their monolithic nature introduces some associated limitations. For instance, potential energy is stored as strain energy in the flexible components, which can lead to stiffness in the relationship between the system's inputs and outputs [8]. There are also challenges in terms of energy efficiency [4] . Dynamics and kinematics require a holistic system analysis and cannot be separated. Moreover, when flexure components undergo significant deformation, control forces and strain forces become nonlinear, which also increases the complexity of system design.

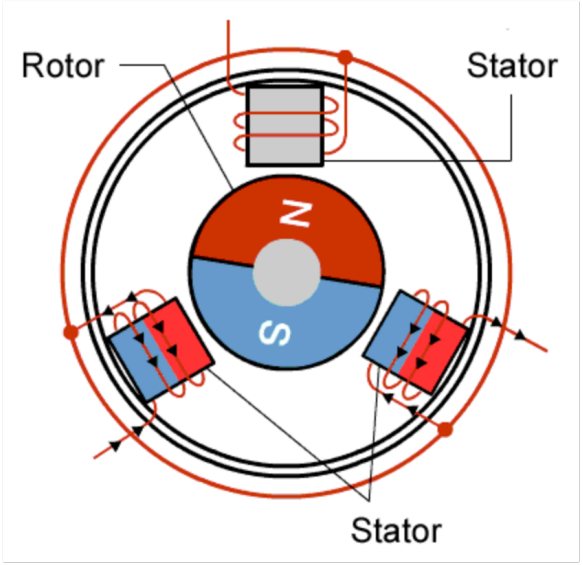

Figure 1.3: BLDC motor[9]

A Brushless direct current (BLDC), also known as a brushless and commutatorless motor, or a synchronous direct current motor, operates with a direct current (DC) input but essentially mimics alternating current (AC) effects by cyclically switching the inverter's main switches. This switching generates a chang-

ing magnetic field within the coil windings, continuously applying torque to the motor rotor, thus keeping it in constant motion [10]. The BLDC is characterized by its high efficiency, high torque, low noise, and low maintenance. As a result, they find application in drive-intensive sectors demanding high performance, such as machine tools, robotics, medical applications. Each arm of the 3-DOF manipulator is driven by a BLDC motors located at the shoulder joint.

A BLDC motor as shown in Figure 1.3 comprises a stator, rotor, and position sensor. The stator consists of laminated steel sheets, with windings placed in slots carved along the internal circular axis. One or more coils are positioned within these slots and interconnected to form the winding. These windings are distributed evenly along the stator's circumference to create uniformly spaced magnetic poles. The rotor of a BLDC motor is equipped with permanent magnets and lacks coils. The north and south magnetic poles of the rotor are alternately arranged. The motor operates based on the principle of magnetic repulsion between like poles and attraction between opposite poles, which causes the rotor to rotate. The primary challenge in controlling BLDC motors lies in accurately determining the rotor's position. There are two methods for rotor position identification. One involves the use of position sensors, such as Hall sensors, to detect the rotor's position. The other method eliminates the need for position sensors and relies on detecting the back electromotive force (EMF) to identify the rotor's position [9]. In the case of RA-PKM, which demands higher precision in position control, so each actuator is equipped with an encoder to detect the motor's position .

However, the test results from previous project turned out that the use of direct drive brushless actuators resulted in significant motion inaccuracies due to cogging behaviour. The cogging effect is visible in the translational motion along the x and y directions, If the end-effector (EE) only performs at constant velocity rotational motion, the cogging effect may not be prominent, but it does indeed have an impact on the motion accuracy of the end-effector [7].

In the case of the BLDC motor, the stator consists of copper wire windings on laminated steel cores, designed to concentrate magnetic flux and enhance torque density. The magnetic poles on the rotor are strongly attracted to the individual steel cores, necessitating torque to align the poles as they move from one set of cores to the next. Therefore, cogging torque arises from the interaction between rotor magnetic flux and variations in stator magnetic reluctance, also known as detent torque, which refers to the force that acts on the rotor of a permanent magnet motor, causing it to have a tendency to come to rest in specific positions when at a standstill. This phenomenon can have a notable impact on the motor's control precision. Additionally, cogging torque induces periodic torque fluctuations, resulting in extra torque ripples and generating undesirable noise, which can affect the motor's overall noise performance. Cogging torque is a persistent presence regardless of the motor's state—whether static or in motion. Cogging torque could potentially lead to vibrations, disrupting the motor's operation and inducing resonant disturbances, which are particularly evident during low speed movement. As a result, the torque pulsations, noticeable during the delicate movements of the manipulator, have the potential to compromise precision. Cogging torque is considered a challenging source of torque ripple to compensate for. Hence, during the motor's design phase, manufacturers take into account using physical design strategies to minimize cogging torque [11]. However, when the motor has already been chosen and in the application phase, utilizing control methods to mitigate the cogging effect is a promising approach grounded in physical optimization.

1.2 LITERATURE REVIEW

Redundant parallel manipulators combine mechanical ingenuity and mathematical complexity. When the number of actuators exceeds the degrees of freedom, a redundant structure is formed within the system. This redundancy aids in eliminating system singularities, but simultaneously, the complexity of system coupling requires more effort to derive the system's equations of motion (EOM) for developing a control strategy. In [12], the use of the Euler-Lagrange equation is proposed for dynamic analysis. In [13], the dynamic equations are obtained using the Lagrange of D'Alembert formulation. However, in [6] and [14], a minimal coordinate method is introduced. This approach is based on the Lagrangian formulation of d'Alembert theorem and employs the principle of virtual work. It combines the advantages of both La-

grange's and Newton-Euler's formulas and eliminates the need for redundant differential operations, as seen in the Lagrangian analysis method.

Meantime, nonlinear kinematics and dynamics are also challenges for system control. How can an effective control strategy be designed and implemented? Consequently, a broad spectrum of control algorithms has been proposed for redundant parallel systems, encompassing augmented PD control[13], computed torque control[2], and nonlinear adaptive control methods[15]. These references predominantly concentrate on achieving better trajectory tracking, which is a pivotal performance indicator for manipulators. Subtle distinctions in joint velocities, EE positions, and dynamic forces have been meticulously examined and leveraged, giving rise to an array of control techniques that enhance the manipulation capabilities of robotic arms.

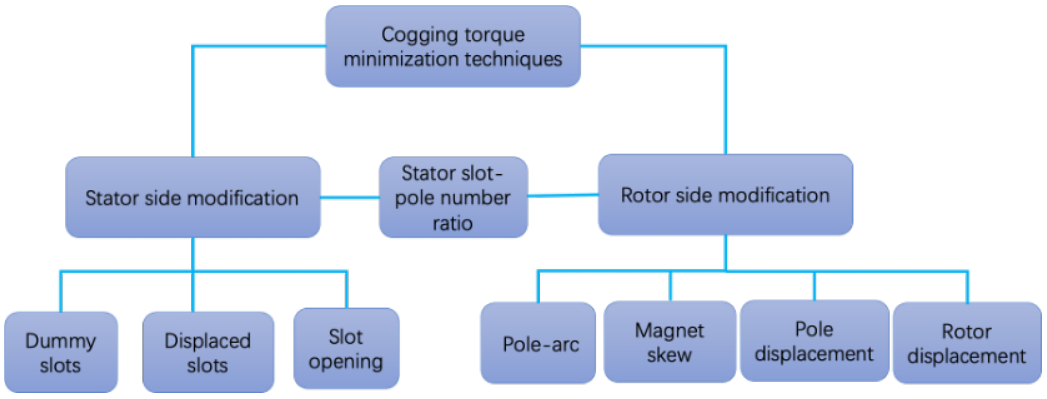

Figure 1.4: Summary of physical design cogging torque minimisation strategies[11][16]

Various approaches can be employed to mitigate cogging torque, primarily falling into two categories: One is based on the physical design of motors, and the other one depends on the control method in the motor. In terms of motor design, several design methods, including geometry optimization, slot/pole number combination method, and stator winding type has been included in [11], [16]. All the classic design techniques are shown in Figure 1.4. Extensive research in motor design has yielded valuable theoretical and practical insights, though implementing these techniques requires tailored designs based on specific product requirements, which may lead to increased production costs. It is crucial to emphasize that cogging torque cannot be completely eliminated through design adjustments. For existing motor products, a promising strategy to further minimize the influence of cogging torque on motion is through advanced motor control techniques. Among these techniques, [17] presents a neural network-based feedforward controller designed to identify and compensate for cogging torque. In [18], both cogging torque and friction are considered external disturbances, and an adaptive robust controller is employed for compensation. In [19], harmonic analysis of motor thrust is introduced to adjust the current waveform and counteract thrust-cogging effects. A flux observer constructed using the Lyapunov direct method was employed in [20], followed by the application of the internal model principle and adaptive feedforward method to suppress torque ripple. The extended Kalman filter was employed in [21] to reduce the cogging torque based on sensorless position control. By combining well-optimized motor design with sophisticated control algorithms, engineers can significantly reduce cogging torque, resulting in improved motor performance, enhanced control accuracy, and reduced noise levels, ultimately offering more efficient and quieter motor operation.

To mitigate the cogging effect, cogging torque model should be obtained to design the control algorithm. There are two types of analysis methods for cogging torque: theoretical analysis and experimental analysis. Theoretical analysis is typically applied during the motor development stage, using finite element analysis to provide relatively accurate cogging torque data. Once the motor selection is confirmed, experimental methods are commonly used to measure cogging torque. There are three methods for torque measurement[22]: (1) using a torque sensor on a professional dynamometer platform, (2) indirectly obtaining cogging torque by measuring current and voltage, and (3) using the electronic scale method. Professional dynamometer

measurement [23] involves connecting the motor to a professional dynamometer, see Figure 1.5(a), and without electric driving, slowly rotating the BLDC rotor to measure the motor's cogging torque using a torque sensor. In this approach, the motor being tested is not powered, while an external stepper motor is employed to induce rotation in the motor being tested, it can calculate the cogging torque by detecting the induced EMF of the stepper motor. The electronic scale [24] measurement method is relatively simple but requires maintaining the balance bar level during the testing process, making the experiment somewhat cumbersome. The method also known as "weight method" [22] allows cogging torque measurement without the need for purchasing specialized testing platforms or professional fixtures, see Figure 1.5(b).

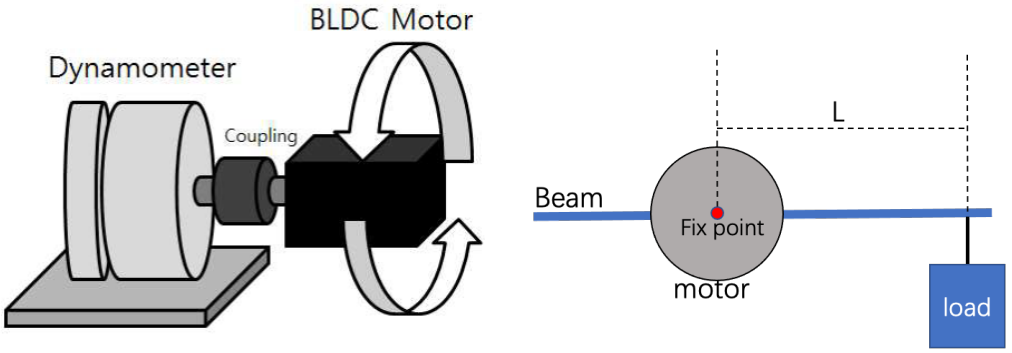

(a) Schematic diagram of dynameter test setting (b) Scheme of measurement setup for gauge method[22]

Figure 1.5: Schematic of measurement setting for cogging torque

1.3 OBJECTIVES OF THE RESEARCH

The literature review reveals that while there are numerous control methods available for RA-PKM, and different control methods to mitigate cogging torque in motors, there is a relatively limited exploration concerning cogging that can affect the redundancy RA-PKM's motion. For instance what function does cogging effect play during the trajectory tracking performance for PKM? Does it indeed influence motion accuracy, particularly during low-speed machine movements? How cogging torque-induced speed/position ripple affects the motion accuracy of the RA-PKM system? Thus this research aims to

- Investigate the cogging model parameters for each motor with parameter identification methods.
- Analyse the influence of cogging torque on the dynamic motion of the PKM.
- Apply control theory knowledge to develop a stable control method to improve the motion accuracy of the manipulator system.

This thesis is organized as follows. Following the introduction part, chapter 2 provides an analysis and modeling of the dynamics and kinematics of the entire 3-DOF manipulator system. Chapter 3 focuses on the introduction of methods for detecting cogging torque, along with the description of experimental setups and the data acquisition methods to figure out the data identification algorithms. Based on the analysis of the cogging torque equation, control algorithms are developed. In Chapter 4, the integration of the cogging torque reduction control method into the manipulator system model and the subsequent testing of the overall system are elaborated. The simulation result takes into account the offset conditions that exist in real tests, and the experimental results are also presented and compared. Ultimately, the thesis wraps up with a thoughtful discussion and conclusion.

Chapter 2

Analysis and modeling of RA-PKM

This chapter is about the analysis of the RA-PKM, with a specific focus on kinematic and dynamic aspects, as well as system modeling and simulation. The kinematics include inverse kinematics and forward kinematic analysis. The dynamic motion analysis is based on the Lagrange method with minimum coordinates, which makes the simulation and modeling easier. To enhance the system tracking performance, a control algorithm has been introduced.

2.1 KINEMATIC AND DYNAMIC ANALYSIS

2.1.1 Inverse kinematic analysis

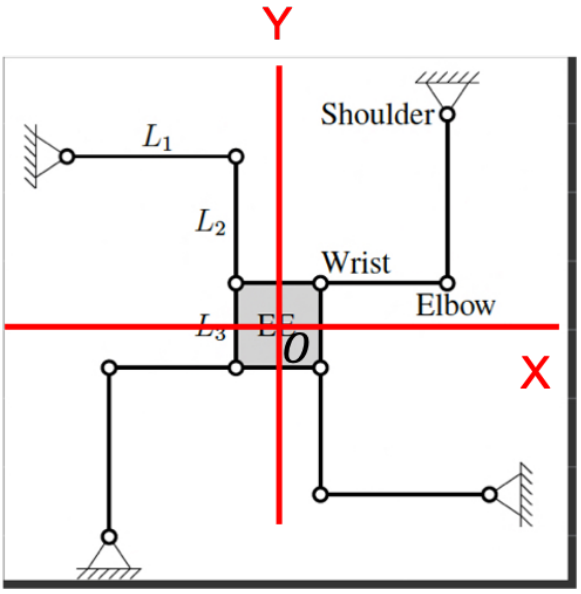

Figure 2.1: Initial configuration of 3-DOF manipulator

The RA-PKM system shown in Figure 2.1 comprises three main components: the end effector (EE), which serves as the moving part (inner square), the fixed part (shoulder part), and four kinematic chains. Each chain has 3 hinges and two links. Four actuators are positioned at the four fixed shoulder joints, each integrated with BLDC motors equipped with encoder sensors to measure the motor's rotation angle. The passive joints are the elbow joints and wrist joints. The original position (frame's zero point) is denoted as O. Since the evaluation of tracking performance is focused on the end-effector, the feedback signal should

be established as the end-effector's position. However, the sensors within this system are situated at the shoulder joints. Hence, the utilization of inverse kinematics becomes necessary to determine the reference angles of the shoulder and elbow. The inverse kinematic involves calculation the joint angle to achieve a desired EE position. This renders inverse kinematics analysis vital for achieving precise control over the end effector's position, thereby ensuring the system's accuracy and efficacy in performing intricate tasks. To realize the intended motion, it is essential to accurately adjust the shoulder joint rotation to attain the desired end effector position. This implies that through the analysis of inverse kinematics results and subsequent dynamic analysis, the force acting on the end effector can be ascertained. The actuator's torque requirements are determined by the force applied to the end effector.

Inverse kinematic solutions can be obtained using analytical methods and geometric methods [1]. In this paper, the geometric method was employed to perform the inverse kinematic analysis [6], which is better to understand and easier to obtain a solution. The initial coordinates of the 3-DOF manipulator were shown in Figure 2.1. A reference frame is established, and the initial position of the inner square center was chosen as the $[0, 0]$ point, so the coordinates for the end effector are $[x_{ee}, y_{ee}, \theta_{ee}]$. Then, the coordinates of 4 wrist joints can be determined. The coordinates of the 4 shoulder joinsts are $[-0.1607, 0.1607]$, $[-0.1607, -0.1607]$, $[0.1607, -0.1607]$, and $[0.1607, 0.1607]$, respectively.

$$
\begin{aligned}
X_{1w} &= x_{ee} + \frac{\sqrt{2}}{2} L_3 \cos\left(\theta_{ee} + \frac{3}{4}\pi\right) \\
Y_{1w} &= y_{ee} + \frac{\sqrt{2}}{2} L_3 \sin\left(\theta_{ee} + \frac{3}{4}\pi\right) \\
X_{2w} &= x_{ee} + \frac{\sqrt{2}}{2} L_3 \cos\left(\theta_{ee} - \frac{3}{4}\pi\right) \\
Y_{2w} &= y_{ee} + \frac{\sqrt{2}}{2} L_3 \sin\left(\theta_{ee} - \frac{3}{4}\pi\right) \\
X_{3w} &= x_{ee} + \frac{\sqrt{2}}{2} L_3 \cos\left(\theta_{ee} - \frac{1}{4}\pi\right) \\
Y_{3w} &= y_{ee} + \frac{\sqrt{2}}{2} L_3 \sin\left(\theta_{ee} - \frac{1}{4}\pi\right) \\
X_{4w} &= x_{ee} + \frac{\sqrt{2}}{2} L_3 \cos\left(\theta_{ee} + \frac{1}{4}\pi\right) \\
Y_{4w} &= y_{ee} + \frac{\sqrt{2}}{2} L_3 \sin\left(\theta_{ee} + \frac{1}{4}\pi\right)
\end{aligned}
\tag{2.1}
$$

$$
\begin{aligned}
r &= \sqrt{(X_C - X_A)^2 + (Y_C - Y_A)^2} \\
\alpha &= \arccos \frac{L_1^2 + L2^2 - r^2}{2 L_1 L_2} \\
\beta &= \arccos \frac{r^2 + L1^2 - L_2^2}{2 L_1 r}
\end{aligned}
\tag{2.2}
$$

$$
\begin{aligned}
\theta_{shoulder} &= \beta + \arctan \frac{Y_C - Y_A}{X_C - X_A} \\
\theta_{elbow} &= \alpha - \pi
\end{aligned}
\tag{2.3}
$$

The following shows the analysis of which one arm is chosen. The position of the shoulder joint is denoted as A, the elbow point is denoted as B, and the wrist joint is denoted C to form a triangle, as shown in Figure 2.2. The coordinate for the 4 wrist joints can be calculated based on the end-effector position Eq.(2.1). Since shoulder joints are fixed, the coordinates for points A and C can be determined, and the distance r

from A to C can be obtained. The angles α and β can be calculated through Eq. (2.2), and finally, the angles of the shoulder and elbow can be obtained through Eq.(2.3).

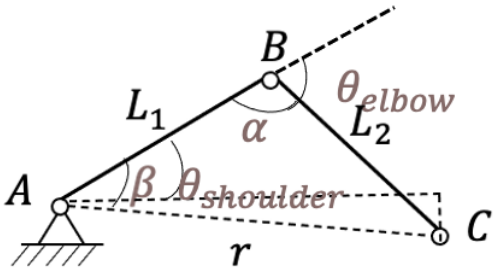

Figure 2.2: Inverse kinematic solution

2.1.2 Dynamic model

The primary objective of conducting dynamic analysis in the parallel manipulator is to obtain the equations of motion. These equations provide crucial insights into the relationships between forces, masses, and accelerations, as well as torques, inertia, and angular accelerations. Understanding these relationships is essential for determining the end-effector forces and consequently calculating the actuator torque required for the system. Once the equations of motion are obtained, the development of system control methods becomes more straightforward and efficient.

In [6], it is mentioned that for multibody systems, there is a method that directly uses independent generalized coordinates to derive the equations of motion. This method uses the minimum number of coordinates, which is equal to the number of degrees of freedom, to represent the motion of the system. Therefore, it is called the "minimal coordinate formulation." In this method, the conversion from independent coordinates to all coordinates is accomplished using the so called geometric transfer function $\mathscr{F}$. The primary goal of motion control is to precisely manipulate the end effector's translational motion in the xy plane and rotational motion θ to meet specific target requirements. Consequently, the entire system's independent coordinates are represented by x_{ee}, y_{ee}, and θ_{ee}. The resulting equation of motion is thus expressed as a function of these independent coordinates with the minimal coordinate method.

In the minimal coordinate formulation, geometric transfer function $\mathscr{F}$ plays a crucial role. Assuming the form of the transformation equations is:

$$q = \mathscr{F}(q_i) \tag{2.4}$$

Where q is the generalized coordinates, while q_i is the independent coordinates.

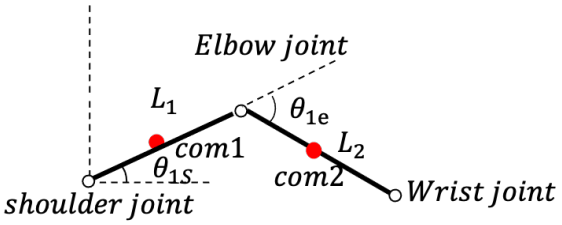

Figure 2.3: Structure of one arm

$$
\begin{aligned}
q = [&x_{1com1} \quad y_{1com1} \quad \theta_{1s} \quad x_{1com2} \quad y_{1com2} \quad \theta_{1e} \\
&x_{2com1} \quad y_{2com1} \quad \theta_{2s} \quad x_{2com2} \quad y_{2com2} \quad \theta_{2e} \\
&x_{3com1} \quad y_{3com1} \quad \theta_{3s} \quad x_{3com2} \quad y_{3com2} \quad \theta_{3e} \\
&x_{4com1} \quad y_{4com1} \quad \theta_{4s} \quad x_{4com2} \quad y_{4com2} \quad \theta_{4e} \\
&x_{ee} \quad y_{ee} \quad \theta_{ee} \quad]^T
\end{aligned}
\tag{2.5}
$$

Based on the system's structure, this manipulator is composed of four chains. Each chain can be considered an independent 3-DOF open-loop system. The overall end-effector is determined by a closed-loop system consisting of four chains and one inner square. Therefore, the dynamic analysis of the parallel manipulator can be carried out by considering the combination of four two-link manipulators and one inner square which means 9 links and each link has 3 coordinates. Consequently, there are 27 generalized coordinates in q. To illustrate the formation of these generalized coordinates, one arm structure, Figure 2.3 was used for each arm coordinate. The length of each link is denoted as L_1 and L_2, while the absolute angles of the joints are denoted as θ_{1s} and θ_{1e}. To facilitate obtaining the inertia of each link, the center of mass for each link is positioned in the middle, represented as red points denoted as $com1$ and $com2$. 27 coordinates characterize the system's motion, including translational movements in the x and y directions and rotational.

To get the equation of $\mathscr{F}$, the holonomic constraint equation should be included. The constraint equations illustrate the limiting relationships that exist between the various links in a PKM system due to their interactions [6]. The RA-PKM system can be viewed as being composed of rigid body arms except the compliant joints, so the system has 27 generalized coordinates, 3 degree of freedom. So there are 24 contraint equations to restrict the motion of the RA-PKM. Hence the holonomic loop constraints equation can be derivated, it is listed in Appendix A equation (A.1). After obtaining the constraint equation, the Jacobian matrix J can be applied to convert the system constraints from geometric to kinematic.

$$
J\dot{q} = (\frac{\partial H}{\partial q})\dot{q} = 0 \tag{2.6}
$$

Generalized coordinates can be divided into independent and dependent parts, as shown in following. The number of degrees of freedom represents the minimum number of coordinates required to describe the system's configuration. The EE coordinates are chosen as the independent coordinates.

$$
\begin{aligned}
q_i &= [x_{ee} \quad y_{ee} \quad th_{ee} \quad]^T \\
q_d &= [x_{1com1} \quad y_{1com1} \quad \theta_{1s} \quad x_{1com2} \quad y_{1com2} \quad \theta_{1e} \quad x_{2com1} \quad y_{2com1} \quad \theta_{2s} \quad x_{2com2} \quad y_{2com2} \quad \theta_{2e} \\
&\quad x_{3com1} \quad y_{3com1} \quad \theta_{3s} \quad x_{3com2} \quad y_{3com2} \quad \theta_{3e} \quad x_{4com1} \quad y_{4com1} \quad \theta_{4s} \quad x_{4com2} \quad y_{4com2} \quad \theta_{4e} \quad]^T
\end{aligned}
\tag{2.7}
$$

Correspondingly, the Jacobian matrix is also divided into two parts: one associated with independent coordinates and the other related to dependent coordinates see Equation .

$$
J_{qd} = \frac{\partial H}{\partial q_d} \qquad J_{qi} = \frac{\partial H}{\partial q_i} \tag{2.8}
$$

By substituting Eq. (2.4) into Eq. (A.1) and differentiate it, Eq. (2.9) can be obtained. Since J_{qd},J_{qi} are known, and $\frac{\partial \mathscr{F}(q_i)}{\partial q_i} = I$, so the expression for $\frac{\partial \mathscr{F}(q_i)}{\partial q_d}$ can be obtained.

$$
\begin{aligned}
H(\mathscr{F}(q_i)) &= 0 \\
J_{q_d}\frac{\partial \mathscr{F}(q_i)}{\partial q_d} + J_{q_i}\frac{\partial \mathscr{F}(q_i)}{\partial q_i} &= 0
\end{aligned}
\tag{2.9}
$$

Using equation Eq. (2.6), first-order geometric transfer function$\mathscr{F}_{,q}$ can be derived as (2.10), which links independent generalized coordinates to all coordinates that describe the geometric behavior of the system [6]. It can be used to convert velocities from generalized coordinates $\dot{q}_d$ to independent coordinate velocities $\dot{q}_i$. I_δ is the identity matrix $I(3*3)$. The matrix $\mathscr{F}_{,q}$ is the orthogonal complement of the Jacobian matrix, the product of the two matrices, identical terms can be canceled [14]. Therefore, using this matrix allows for obtaining the minimal coordinate representation of the system.

$$\begin{aligned} q = \mathscr{F}(q_i) \quad \dot{q} = \mathscr{F}_{,q}(q_i)\dot{q}_i \\ \mathscr{F}_{,q} = \begin{bmatrix} -J_{qd}^{-1}J_{qi} \\ I_\delta \end{bmatrix} \end{aligned} \tag{2.10}$$

$$\begin{aligned} M = diag(M_{1u} \quad M_{1l} \quad M_{2u} \quad M_{2l} \quad M_{3u} \quad M_{3l} \quad M_{4u} \quad M_{4l} \quad M_{inner}) \\ f = [f_{xiu} \quad f_{yiu} \quad \tau_{iu} \quad f_{xil} \quad f_{yil} \quad \tau_{il} \quad f_{xee} \quad f_{yee} \quad \tau_{\theta ee}] \end{aligned} \tag{2.11}$$

To derive the equation of motion of the system, considering the Newton-Euler equation, the system inertia matrix M and force vector f should be introduced. M is a diagonal matrix, each body contains 3 inertia variables, which are the center of mass lumped masses and the rotational inertia about the center of mass [6]. The system consists of 4 upper M_{iu} and lower armsM_{il} and an inner squareM_{iner}, so the dimension of the inertia matrix is 27×27. M is a 27-diagonal matrix. f refers to the force or torque acting on the center of mass. Since this is a planar system, gravity can be ignored, and only the stiffness torque in the rotational direction is considered. The system has 9 joints with stiffness, so f is a 27×1 matrix.

$$\bar{M}(q)\ddot{q}_i + \bar{C}(q,\dot{q})\dot{q}_i + \bar{Q}(q) = \epsilon_{,q}^T \tau \tag{2.12}$$

where

$$\bar{M} = \mathscr{F}_{,q}^T M \mathscr{F}_{,q}, \quad \bar{C} = \mathscr{F}_{,q}^T M(\mathscr{F}_{,qq}\dot{q}), \quad \bar{Q} = \mathscr{F}_{,q}^T f \tag{2.13}$$

Based on the Newton-Euler equations and utilizing the generalized D'Alembert's principle, for rigid multibody systems, which is essentially the principle of virtual work, the general form of the minimal coordinate equations is expressed as Eq. (2.12), In Eq. (2.12), τ represents the actuator torque at the shoulder joint, which can be converted to the end effector force through matrix $\epsilon_{,q}$. This matrix is a subset of matrix $\mathscr{F}_{,q}$ reveals the relationship between the shoulder angles $[\theta_{1s}, \theta_{2s}, \theta_{3s}, \theta_{4s}]$ and the position of the end effector $[x_{ee}, y_{ee}, \theta_{ee}]$.

As the values of M and f have been acquired through the system, the EOM can be obtained.

The parameters for this manipulator system are shown in Table 2.1, which can be used to perform the simulations.

Table 2.1 Parameters of the manipulator

	Shoulder	Elbow	wrist	unit
Armlength	0.1282		0.065	$[m]$
Stiffness	0.01	0.05	0.04	$[Nm/rad]$
ArmMass	0.05	0.041	$0.0391(innersquaremass)$	$[kg]$
Joint Mass	0.019	0.053	0.039	$[kg]$
Inertia	0.00014	0.00013	0.000076	$[kg.m^2]$

2.1.3 Actuator torque allocation

From the minimal coordinate equation, the end effector force can be obtained as $\epsilon_{,q}^T \tau = F_e$, F_e is the applied force on EE. In the case of a non-redundant system, the solution for the actuators can be straightforwardly obtained $\tau_{actuator} = inv(\epsilon_{,q}^T) F_e$. For this RA-PKM mechanism, the number of actuators exceeds the number of system dynamic equations. This indicates that three equations are available to solve for four unknowns. Therefore, an optimization approach is needed to find the solution.

In practical applications, the distribution of actuator forces is closely related to controller design. Considering the ease of implementation in practical control scenarios, the minimum 2-norm [7] has been employed to obtain the optimal solution. The optimization of redundant actuator torque distribution using the minimum 2-norm aims to minimize the actuator energy consumption and the constraint equation is Eq. (2.12). Since the purpose of the optimization is to minimize energy, the optimization objective function can be set as $O_f = W\tau^2$, where W is a positive definite diagonal weighting matrix. Following the above analysis, the Lagrange multiplier method in [25] is employed to solve for the driving torques. performance index function can be defined as Eq. (2.14), where λ represents the Lagrange multiplier. The optimization problem for actuator torques becomes a problem of finding the extremum of a multivariate function.

$$O_{fi} = W\tau^2 + \lambda^T (F_e - \epsilon_{,q}^T \tau) \tag{2.14}$$

Taking partial derivatives of the Eq. (2.14) with respect to τ and λ, and setting to zero, the following equations are obtained:

$$\frac{\partial O_{fi}}{\partial \tau} = 2W\tau - \epsilon_{,q}\lambda = 0 \tag{2.15}$$

$$\frac{\partial O_{fi}}{\partial \lambda} = F_e - \epsilon_{,q}^T \tau = 0 \tag{2.16}$$

Since W is positive definite diagonal, so it is invertible, From Eq. (2.15) τ can be written as.

$$\tau = \frac{1}{2} W^{-1} \epsilon_{,q} \lambda \tag{2.17}$$

By substituting τ from Eq. (2.17) into Eq. (2.16), λ is:

$$\lambda = 2(\epsilon_{,q}^T W^{-1} \epsilon_{,q})^{-1} F_e \tag{2.18}$$

Finally the equation for τ becomes:

$$\tau = W^{-1} \epsilon_{,q} (\epsilon_{,q}^T W^{-1} \epsilon_{,q})^{-1} F_e \tag{2.19}$$

When the weight matrix varies, the solutions obtained will also differ. This method is primarily based on the minimum 2-norm approach, so the weight matrix is taken as the identity matrix. Therefore, the equation can be simplified into

$$\tau = (\epsilon_{,q}^T)^{\dagger} F_e \tag{2.20}$$

where $(\epsilon_{,q}^T)^{\dagger} = \epsilon_{,q}(\epsilon_{,q}^T \epsilon_{,q})^{-1}$ denote the (Moore-Penrose) pseudoinverse of $\epsilon_{,q}^T$.

2.1.4 Forward kinematics analysis

According to the previous analysis, the coordinates of the other joints required to reach the target terminal position are obtained through inverse kinematics analysis. By performing dynamic analysis, the end-effect force can be calculated, and the driving forces of the four motors can be obtained through the operation of the Jacobian matrix least square method. The angle output on the shoulders is measured by the encoder. However, the position of the end effector cannot be directly measured by the sensor. Hence, it is necessary to employ forward kinematics to calculate the position of the end effector.

Because the shoulder angle has been measured using the encoder, it becomes possible to calculate the position of the elbow. Constraint equations only include the elbow, wrist, and end effector. These equations are the last 8 items of the constraint equations for the whole system in Appendix A Eq. (A.1), which denoted as $S(q_s)$, $q_s = [\theta_{1e}, \theta_{2e}, \theta_{3e}, \theta_{4e}, x_{ee}, y_{ee}, \theta_{ee}]$ is the nominal parameters which including 4 elbow angles and 3 EE position.

$$q_s(i+1) = q_s(i) - (\frac{\partial S(q_s)}{\partial q_s(i)})^{\dagger} * S(q_s) \tag{2.21}$$

With the Newton-Raphson method in [6], which is based on the initial point, drawing a tangent line at that point, and determining the coordinates of the next iteration point where the tangent line intersects with $q_s - axis$. This process is then repeated at the new point, and so on until an approximate solution satisfying the desired accuracy is obtained. The Eq. (2.21) is introduced to get the EE position. Because of the redundant system, there are more constraint equations than coordinates of vectors, 8 constraints equation and 7 unknown parameters vector, so use pseudoinverse to get the derivation of the constraint equation. Position Forward kinematics involves determining the position of the EE position given the known input angles of the active joints. In practical applications, it can be used for real-time monitoring the EE position in control systems. Therefore, the efficient solution of position-forward kinematics is significant for the control of parallel robots. To achieve this efficiency, the number of Newton's iterations is set to one step in Simulink model. Through simulations, Figure 2.4 has been demonstrated that this approach can get an actuate EE position based on the input angles.

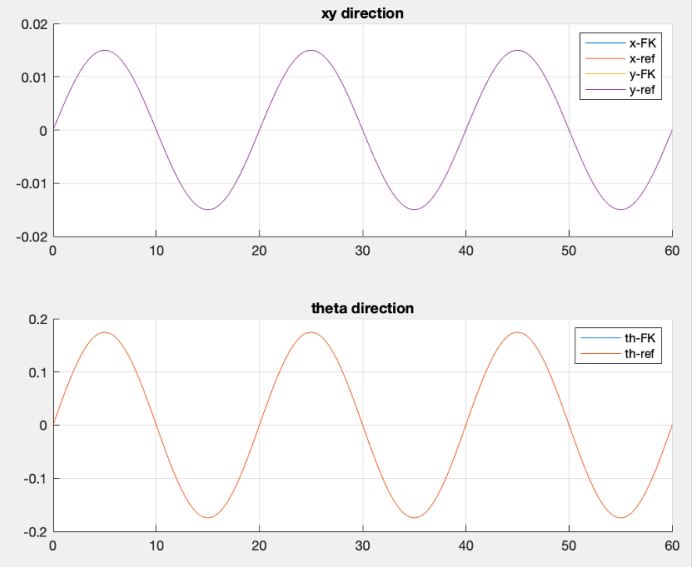

Figure 2.4: comparison of reference and forward kinematics calculation

2.2 PKM SYSTEM CONTROL

In literature, for parallel manipulators, there are two basic control methods, one for the kinematic control method and another for is dynamic control method[12]. Kinematic control strategy includes Proportional-Integral-Derivative control (PID) controller. To simplify the development of the controller, Assume that the system has independent input and output. Experimental tests in [7] have shown the viability of this decoupling method. A multi-input multi-output(MIMO) system is simplified into three single-input single-output(SISO) systems, with the inputs being the position errors in the x, y, and rotation directions, and the outputs being the external forces at the EE.

The feedback PID controller transfer function is

$$K(s) = k_p \frac{s\tau_z + 1}{s\tau_p + 1} \cdot (1 + \frac{1}{\tau_i s}) = k_p \frac{(s\tau_z + 1)(s\tau_i + 1)}{s\tau_i(s\tau_p + 1)} \tag{2.22}$$

$$k_p = \frac{m_{eq}\omega_c^2}{\sqrt{\frac{1}{\alpha}}} \tag{2.23}$$

$$\tau_p = \frac{\sqrt{\alpha}}{\omega_c} \tag{2.24}$$

$$\tau_z = \frac{1}{\omega_c\sqrt{\alpha}} \tag{2.25}$$

$$\tau_i = \beta\tau_z \tag{2.26}$$

In[26] all parameters can be expressed in desired cross-over frequency ω_c. Based on the calculation method of the crossover frequency in the [26], we determined the crossover frequency for each degree of freedom, considering system stability, $5Hz$ is chosen as the crossover frequency. β is an integral action, the suggested value is ≥ 1, as it is helpful to increase the phase margin at cross-over frequency, so choose 1. Phase lead α between 0.1 and 0.3, β is larger than α because the phase lag of the integral action should not affect the phase lead of the derivative action. so chose $\alpha = 0.1$. Given m_{eq} is the equivalent inertia for the system, the overall system possesses an equivalent mass matrix $(\bar{M})$ consisting of 3×3 terms. This can be achieved by the multiplication of the plant with reduced mass $\bar{M}$ and it is deemed valid when the product $\bar{M}$ and $Plantequation$ results in a diagonal transfer matrix with an approximate $\frac{1}{s^2}$ on the diagonal, particularly in the vicinity of the cross-over frequency [7]. so setting $m_{eq} = 1$ in this case.

The PID controller parameter can be obtained through the above setting, the final parameter is shown in Table 2.2.

Table 2.2 Parameters of PID controller

Parameters	value
m_eq	1
ω_c	$5Hz$
k_p	312.1043
τ_p	0.0101
τ_i	0.1007
τ_z	0.1007

In consideration of system stability, it is essential to ensure that the crossover frequency remains within a specific, predetermined range [27]. To further improve the precision of system motion, feedforward control is also employed in the control method. To achieve better dynamic performance, the equation for the feedforward control should be the inverse of the plant's transfer function. In the section on dynamic motion analysis, the plant model has already been calculated in Eq. (2.12), with the reference end-effector position, so the end-effector force can be obtained. With the geometric subset transfer function $\epsilon_{,q}$, optimal actuator torque can be yielded through with Eq. (2.20).

2.3 SIMULATION AND MODELING

Once the system model and control method are established, the initial step is to conduct simulations to test the effectiveness of the control method, plant model, and actuator torque allocation.

The model structure is depicted in the Figure 2.5, with each module fulfilling different functions, corresponding one-to-one with the Simulink model Figure 2.6. Firstly, the target trajectory is set up using sine functions for both $x - y$ and rotation. Velocity and acceleration are also defined for this trajectory. Based on [7] workspace calculations, the x and y target amplitudes are set to 0.015m, with a frequency of 0.05Hz, while the rotation amplitude is 10 degrees, with the same frequency. The target trajectory is loaded from a Matlab script.

To compare the reference trajectory with the position obtained from sensors (the EE position is calculated through forward kinematics, using the shoulder position obtained from the encoder). The PID controller Eq. (2.22) adjusts the output force (i.e., the control variable) based on the error. Simultaneously, in the feedforward control loop, the desired positions for each joint are obtained through inverse computations Eq. (2.3). With the joints angles and EE reference position, velocity and acceleration, can get the $\bar{M}, \bar{C}$ and $\bar{Q}(q)$, using the minimal function (2.12), the feedforward control variable (EE force) can also be calculated. The two are added together to form the final control input. However, at this time, the output dimension for the control force is 3×1, and it needs to be transformed into the demands for the four actuators through the minimum 2-norm operation Eq. (2.20) in the force to torque diagram (Dimension from 3×1 to 4×1).

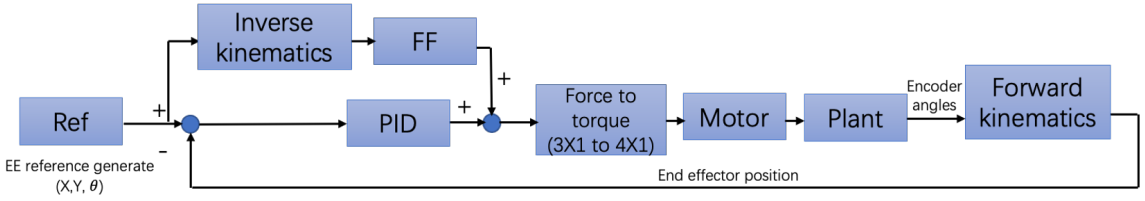

Figure 2.5: Structure of model

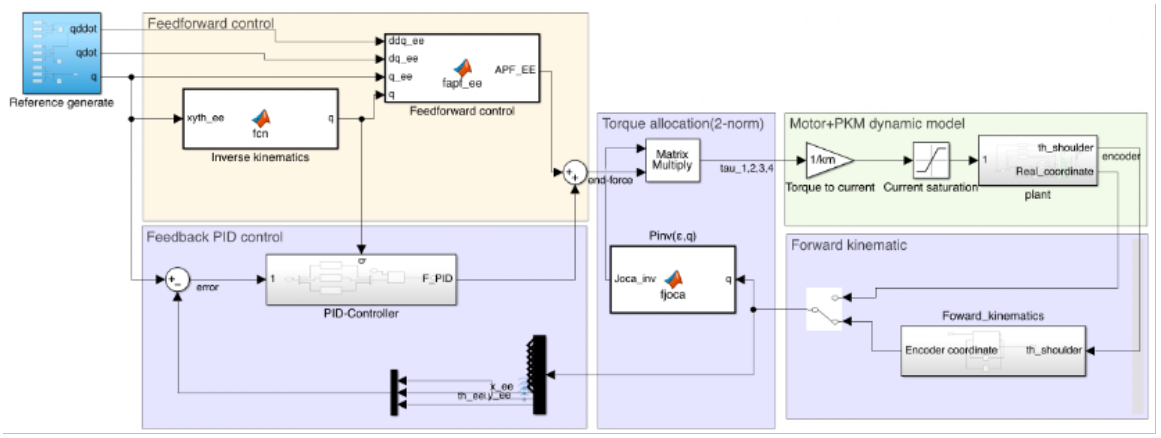

Figure 2.6: Diagram of manipulator simulation model

After ensuring the torque allocation for the 4 actuators, the required torque serves as input parameters for the motor model. However, in practical applications, motor input parameters are typically current or voltage. The setup for the real test platform also uses current drives. Since this study does not focus on detailed motor modeling, using the torque constant k_m to complete the conversion from torque to current is sufficient. For safety reasons in practical applications, motors have working current limits, so saturation limits are added to restrict the current range at the current output end. Finally, the current demand is input into the plant model. The plant model is a sub-model, the block diagram shown Figure 2.7. First, the current is converted into the actuator's torque output using the torque constant. This drive torque is then transformed into forces acting on the three degrees of freedom at the end of the EE through the first order

transfer function $\epsilon_{,q}$ from shoulder to EE. The reaction force caused by stiffness and Coriolis effects are subtracted by the end drive force to calculate the EE applied force. Once the EE force is determined, it is multiplied by the inverse of the reduced inertial matrix M to calculate the acceleration of the three degrees of freedom. By integrating the acceleration over time, the EE's velocity is obtained. To compute the velocities of all joints, the system's Jacobian matrix $\mathscr{F}_{,q}$ comes into play. Starting with the initial configuration of the system as the initial condition for the integral then coordinates for the entire system can be determined. The shoulder angles, which act as inputs are utilized, in the forward kinematic calculations to deduce the position of the EE. This integrated process allows us to control the manipulator and achieve the desired movements effectively.

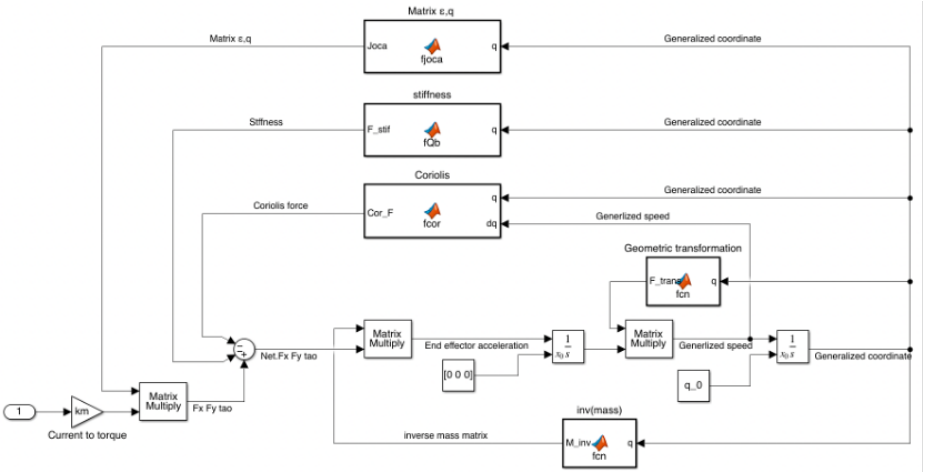

Figure 2.7: Plant model

Chapter 3

Cogging torque analysis

The main purpose of this chapter is to determine relevant parameters and establish the cogging torque testing method through an analysis of the general formula for cogging torque. Based on the data obtained from the testing, the cogging torque will be systematically identified. Subsequently, a control algorithm will be developed using the identified torque formula to enhance motion accuracy.

3.1 COGGING TORQUE EQUATION

To control the cogging torque, it is essential to have a sufficient understanding of it, particularly its mathematical expression. This expression can show the design and control parameters that affect the cogging torque. Currently, various electromagnetic simulation software can accurately calculate the cogging torque using finite element analysis. However, since motors are three-dimensional objects, constructing a 3D model requires significant computer resources, computation time, and detailed knowledge of the motor parameters, making it less universally applicable [11]. An alternative to Finite Element Method is analytical methods [11], which can reduce the computational load on computers and save processing time . Although the analytical analysis method may not consider effects such as saturation and leakage flux, However, the purpose is to obtain corresponding parameter determination methods to design and optimize the cogging torque, rather than achieving precise calculations.

Cogging torque is the torque generated by the interaction between the permanent magnet and the iron core of the permanent magnet motor's winding when it is not energized. It is caused by the tangential component of the interaction force between the permanent magnet and the stator slots. When there is relative motion between the stator and rotor, the magnetic flux between the armature teeth in the permanent magnet pole arc region remains relatively constant. As a result, the magnetic field around these armature teeth remains relatively unchanged. However, in the small region corresponding to the two sides of the permanent magnet, constituted by one or two armature teeth, the magnetic flux changes significantly, leading to variations in magnetic energy and consequently resulting in cogging torque. Cogging torque is defined as the minus derivative of the magnetic field energy E with respect to the relative angular position θ of the stator and rotor when the motor is not energized. This can be represented as:

$$T_{cog} = -\frac{\partial E}{\partial \theta} \tag{3.1}$$

Based on the following assumption:

- The armature's iron core permeability is assumed to be nearly infinite;
- The permanent magnet's properties within the same motor are identical and evenly distributed;
- The permeability of the permanent magnet is considered to be the same as air;
- The stacking factor of the iron core is 1.

The expression for the cogging torque can be derived [28]:

$$T_{cog}(\theta) = \frac{\pi z L_s}{4\mu_0}(R_2^2 - R_1^2)\sum_{n=0}^{\infty} nN_L G_n B_r \sin(nz\theta) \tag{3.2}$$

In the equation, L_s is the stack length, z is the static number, μ_0 is the air permeability, R_2, R_1 denoted stator bore radius and magnet outer radius, while G_n, B_r are coefficients of the air gap function and flux density function. N_L is the least common multiple of the motor's stator slots and rotor poles. The period of the cogging torque is $\frac{2\pi}{N_L}$[29], and the unit is rad which means the cycle has a relationship with the rotor angle θ.

In [30] and [31], under the assumption of neglecting the iron saturation and end effects, the expression for cogging torque is represented using the superposition principle through a Fourier series Eq.Equation 3.3.

$$T_{cog}(\theta) = \sum_{n=1}^{\infty} T_k \sin(kz\theta + \phi_k) \tag{3.3}$$

T_k, ϕ_k represent the amplitude and phase shift of the k_{th} order, respectively. Normally the number of Fourier series k can be defined as 4, which can give a good approximation for cogging torque [30].

From the equations for cogging torque, it is evident that the cogging torque's magnitude is influenced by the motor's position. Equation (3.2) clearly expresses the possibility of reducing cogging torque through design choices related to the motor. This implies that during the initial motor design phase, engineers can proactively consider methods such as fractional pitch, skew of the magnet, pole arc to pole pitch ratio, and others to minimize cogging torque based on the specific application requirements. Finite element analysis can be employed to calculate the cogging torque once the motor design parameters are confirmed.

Moreover, Eq. (3.3) offers a means to devise a cogging torque testing method. By knowing the number of stator slots, the cogging torque can be identified through testing the motor's position and output torque. This enables a comprehensive evaluation of cogging torque during the motor's performance analysis and optimization stages.

The actuators for the redundant parallel manipulator system are identical to those used in [7]. The specific parameters are provided in the Table 3.1.

Table 3.1 Motor specifications

Variable	Value	unit
Norminal torque	387	$[mNm]$
Torque constant	70.5	$[mNm/A]$
Pole pairs	12	
Encoder resolutions	25600	$[counts/rev]$
Motor mass	0.6	$[kg]$
Motor radius	0.045	$[m]$
Rotor inertia	3060	$[gcm^2]$

3.2 COGGING TORQUE DATA MEASUREMENT

3.2.1 Test platform setting

In general, cogging torque data collection is a critical process that demands accurate measurements. Traditionally, it involves the utilization of specialized torque sensors or dynamometers, which are designed to

provide precise and reliable readings of torque output. Additionally, precision electronic scales, weights, and fixtures are employed to ensure the stability and reproducibility of the experiment, similar to the approach described in [24]. These will lead to an increase in costs, sometimes even more expensive than the motor being used. Considering that the ultimate target of the test results is a parallel manipulator system, meanwhile a relevant experimental platform has been set up by previous students, this data collection experiment is designed based on existing resources. Moreover, using the existing platform allows for continuity and consistency in the testing process, reducing the likelihood of introducing additional variability.

The experimental platform has been thoughtfully divided into two distinct setups to comprehensively assess the motor's performance. The first part exclusively targets the motor, independent of any external mechanical elements like a robotic arm. This configuration enables the motor to undergo a complete revolution, capturing data throughout the entire 2π cycle, so the data can be obtained at every angle. The second set focuses on investigating the motor's behavior when integrated with one arm. In this setup, the motor's motion is constrained within a limited range, specifically within the interval of $[-10, 10]$ degrees, due to structural limitations imposed by the one-arm mechanism. By analyzing the data from both platforms, it is possible to dissect the information contained within the measured torque, such as the stiffness part, friction part, and other relevant components.

3.2.2 Experiment setting

The torque ripple, comprising cogging torque, friction torque, inertia, and stiffness torque from other components, is a critical indicator of the motor's performance and efficiency. In the first test platform, which concentrates solely on the motor itself, a comprehensive full rotation test is conducted. This test captures the torque ripple data across the entire 360-degree angular range. By collecting torque data throughout a complete rotation, the periodic movement characteristic of the cogging effect can be observed. Also the friction torque, which arises due to mechanical resistance in the motor's bearings and other moving parts, can be measured and analyzed during this test. On the other hand, the second test platform, the motor with the one-arm test, introduces a practical constraint by restricting the motor's motion within the mechanical structure, limited to the range of $[-10, 10]$ degrees. By examining the torque ripple under these constrained conditions, the influence of stiffness can also be observed. In order to distinguish the different components of torque ripple more effectively, both test platforms are designed with target motion trajectories that include both forward and reverse movements. This choice is made because, for a motor, the direction of friction force can vary between forward and reverse motions, while cogging torque is solely dependent on the motor's position. The cycle's motion trajectory also includes circular movements with different motion periods. This enables the observation of torque ripple characteristics under various motion cycles.

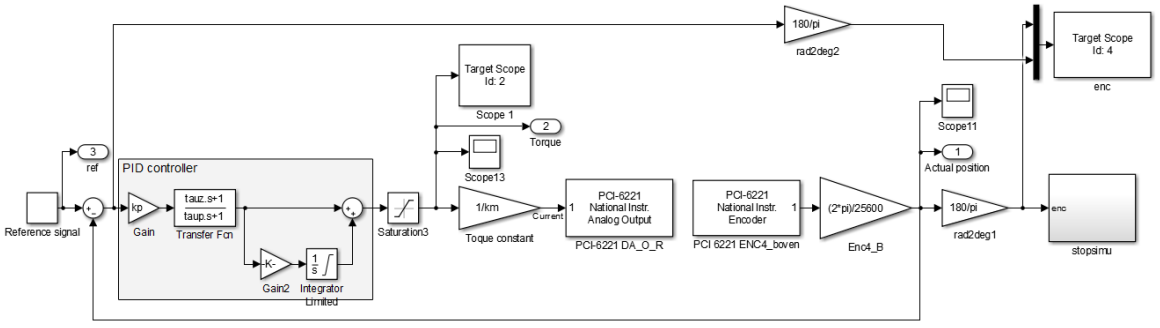

Figure 3.1: Structure of real-time torque data collection model

For the position-based torque ripple collection method, one might consider performing the constant velocity open-loop test to observe the motor's behavior, where no acceleration inputs in to the system, therefore, no model inertia. However, it is essential to recognize that open-loop tests lack the necessary

feedback mechanism to ensure precise and consistent motion. Consequently, the motor's rotation may not achieve the required uniformity, leading to inaccurate or incomplete torque ripple data. This limitation makes it challenging to distinguish between the contributions of various torque components. To address these challenges and ensure accurate results, a closed-loop control experiment with a PID controller is employed. In this setup, the motor's position is continuously monitored through a feedback sensor, allowing the PID controller to make real-time adjustments to maintain the desired position and achieve precise uniform rotation. By employing the closed-loop PID control experiment with feedback, high-quality torque ripple data can be obtained. This data is helpful for conducting a more detailed analysis of the motor's behavior and optimizing the motor's efficiency for the RA-PKM.

Figure 3.1 shows the structure of the real-time torque data collection model, the repeating sequence block generates the reference trajectory of Figure 3.2 for the motor. The actual position signal from the encoder is subtracted from this target trajectory to calculate the error. The PID control is then applied to adjust the motor's output torque. The PID parameters are obtained with Eq.(2.22). Chosen ω_c as $30Hz$, m_{eq} is the moment of inertia of the motor, which can be derived through motor parameters in Table 3.1, $\alpha = 0.1$, $\beta = 2$. To ensure the motor's safety, torque limits are set using a saturation block, preventing the torque from exceeding specified upper and lower bounds. Additionally, the input motor current is calculated using the torque constant, denoted as k_m. This constant allows for the conversion of torque into the corresponding motor current. $Out1$ denotes the motor angle measured by the encoder, providing real-time feedback on the motor's actual position. $Out2$ represents the torque output calculated by the PID controller. This torque output serves as the control signal required to keep the motor aligned with the desired trajectory, effectively guiding the motor's motion toward the target position. By continuously comparing the encoder-measured angle ($Out1$) with the desired trajectory and generating the appropriate torque output ($Out2$), the PID controller ensures accurate and stable motor positioning throughout the operation.

To achieve control and testing of the motor's internal torque and position, both hardware and software setup are required for the system. A desktop PC operates as the target PC, running a Real-Time operating system and executes the Simulink model. Communication between the desktop PC and the motor controller is established through an encoder which includes amplifiers and sensors as an interface. The specific model of the encoder card is NI PCI-6221. The encoder can transmit the motor angle to the target PC, serving as feedback signal for the system. While the current demand computed within Simulink and converts it into an analog signal through DAC in NI PCI-6221 can output current, serving as the input to the motor.

3.3 COGGING TORQUE IDENTIFICATION

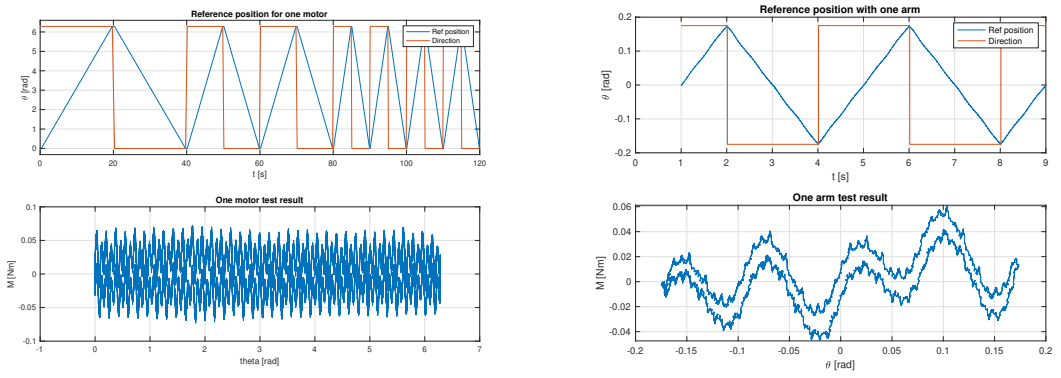

(a) (b)

Figure 3.2: (a)Cycle test map and result (b)One arm test map and result

Through the test platform and experimental design outlined in the previous section, two sets of data can be obtained. These datasets encompass motor rotation angle and torque output. Since the motion is constant speed trajectory tracking, the reference position has been shown in Figure 3.2, so acceleration is always 0, if the data near the velocity direction change is deleted, the influence of inertia can be disregarded.

In order to facilitate data analysis and due to the presence of noise in the initial data, filtering was applied to the torque data. The test results show in Figure 3.2 that the motor-with-one-arm platform, due to its strong correlation between torque and motor rotor position, certainly includes stiffness torque. By analyzing the torque differences between forward and reverse directions in both the motor-only and motor-with-one-arm tests, the presence of friction torque can be inferred. With the exclusion of the torque components' effects, it becomes apparent that cogging torque manifests as periodic motion, with a torque period of 5 degrees, and the rotor's pole pairs are 12 which are listed in the motor specification. According to the above test results analysis, the torque component included in the fitting function for testing torque is the sum of all the sub-torque functions mentioned above, and its function in the form

$$f(\theta) = P_1 + P_2\theta + P_3\dot{\theta} + P_4 sign(\theta) + \sum_{i=1}^{m} P_{i+4}\sin(n_{poles}i\theta) + \sum_{i=1}^{m} P_{i+m+4}\cos(n_{poles}i\theta) \tag{3.4}$$

$$g(\theta) = [I \quad \theta \quad \dot{\theta} \quad sign(\theta) \quad \sin(n_{poles}i\theta) \quad \cos(n_{poles}i\theta)]^T \tag{3.5}$$

Finally, the fitting function is Eq. (3.4), where the correlation coefficient P signifies the relative contribution of various torque ripple components within the test results, $P = [P_1, P_2..., P_4 + 2m]$. The basic function is Eq. (3.5), where I is the identity matrix, and the size is the same with measured motor position θ. This approach enables an assessment of the diverse torque ripple elements, to analyze which factors contribute more to the torque ripple, and to determine which harmonic has a greater influence on the cogging torque.

The composition of this fitting function (3.4) involves the linearization of various components within the torque ripple. The fitting function is composed of offset, stiffness torque, viscous friction torque, Coulomb friction torque, and cogging torque. The stiffness torque equation is represented as $k\theta$, where stiffness is a constant term and θ signifies the angular displacement. Viscous friction is correlated with velocity $\dot{\theta}$, while Coulomb friction is influenced by the direction of motion $sign(\theta)$, forming the first four terms of the fitting function.

$$f_{CT}(\theta) = \sum_{i=1}^{m} P_{i+4}(n_{poles}i\theta) + \sum_{i=1}^{m} P_{i+4+m}(n_{poles}i\theta) \tag{3.6}$$

The subsequent terms within the fitting function pertain to the representation of cogging torque. Cogging torque is assumed to be periodic such that it can be defined as composed of numerous harmonics. Drawing insights from the earlier analysis of cogging torque, a Fourier series is employed as the fitting formula. This formula encompasses functions of amplitude and frequency. The frequency component is deduced through the Fourier transform of the data, yielding the system's fundamental frequency and dominant frequency. By analyzing the frequency spectrum [32] of the test torque, harmonic frequency data can be extracted, denoted as m, which represents the number of harmonics, the upper limit for the summation ($\sum$). The spectrum result for the ripple torque is shown in Figure 3.3, and the analysis is based on a single-arm test result, with a constant speed of 0.087 rad/s. The spectrum results show one dominant competent at $125Hz$, and the other 5 components have almost the same amplitude which less than almost 10% of the dominant one. So the harmonic number can be chosen as 6 which is shown in red circles in Figure 3.3, while the number of poles for the motor is already known from the motor parameters which is 12. The cogging torque equation can be obtained.

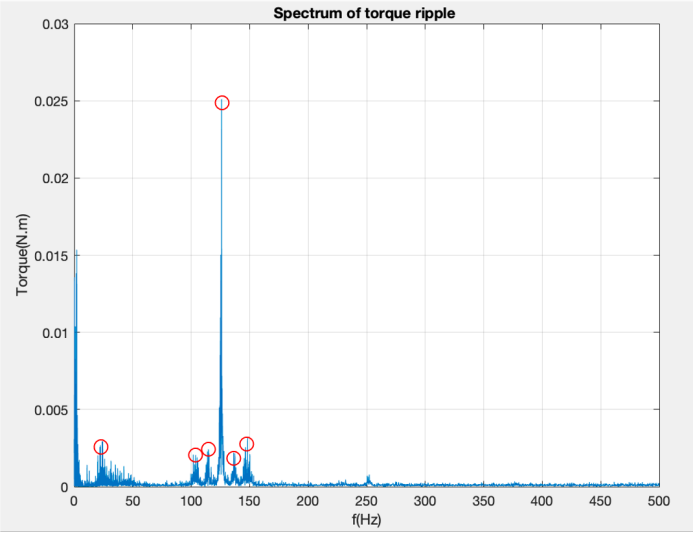

Figure 3.3: Spectrum of torque ripple

Because $f(\theta)$ is an approximate function for testing torque, by assuming $f(\theta) = \tau_{test}$, the test torque has been obtained from the previous section. The parameter P can be determined. By evaluating the values of the parameter, this analysis allows for the assessment of the significance of each component's presence in the torque ripple. Furthermore, the calculation of cogging torque will also be obtained.

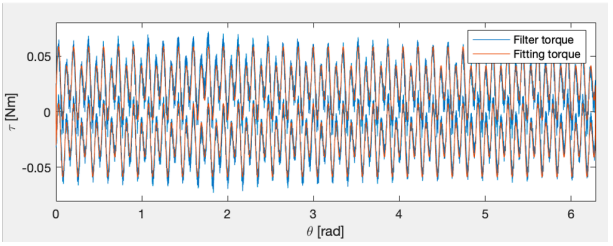

(a)

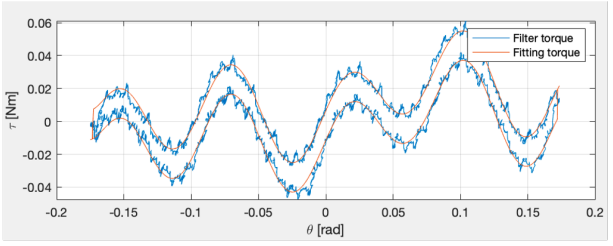

(b)

Figure 3.4: (a)No arm fitting result (b)One arm fitting result

For the free-running motor test result shown in Figure 3.4 (a), the computed results indicate that the weighting proportion of stiffness is notably low, approximating nearly zero in comparison to other components. Additionally, within the cogging torque, the dominant harmonics are primarily the third and sixth terms. Consequently, the elements of the weighting function can be simplified to seven terms. Among these, four terms are associated with cogging torque's harmonics, while the remaining terms encompass offset, viscous damping, and Coulomb friction components. The one-arm test result in Figure 3.4 (b) ap-

parently includes friction and stiffness. From the fitting results, it can be seen that the torque fitted using this identification method aligns well with the measured torque. Therefore, this identification result can be used as the motor's torque ripple, and a corresponding mitigation control method can be designed based on this.

The identification results is the free motor identification which has no stiffness.

$$\begin{aligned} f(\theta) = 7.6 \times 10^{-5} + 0.0014\dot{\theta} + 0.0246 sign(\theta) + 0.038\sin(12\cdot 3\theta) + 0.0186\sin(12\cdot 6\theta) \\ +0.0118\cos(12\cdot 3\theta) - 0.0144\cos(12\cdot 6\theta) \end{aligned} \tag{3.7}$$

The identification result is for motor with one arm.

$$f(\theta) = 0.048 - 7.93\theta - 0.055\dot{\theta} + 0.014 sign(\theta) + \sum_{i=1}^{6} P_{i+4}\sin(n_{poles} i\theta) + \sum_{i=1}^{6} P_{i+m+4}\cos(n_{poles} i\theta) \tag{3.8}$$

$$P(5:16) = [1.23 \quad -0.47 \quad 0.21 \quad -0.079 \quad 0.021 \quad 0.021 \quad -0.084 \quad 0.066 \quad -0.055 \quad 0.024 \quad -0.012 \quad 0.01]$$

The result encompasses the influential factors of arm stiffness, since the one-arm test has physical rotational range limitations and insufficient data collection, the identified cogging torque does not match the expected sinusoidal waveform. Therefore, the cogging compensation equation from the free motor identification results is selected and integrated into the simulation model for simulating cogging effect. This, in turn, serves as the foundation for our control algorithm design.

3.4 CONTROL METHOD DESIGN

3.4.1 Control method design

There are various methods available to reduce cogging effects in motors, but most of them require modifications to the motor design. One approach involves equipping the motor with an encoder. By knowing the motor's precise position, the motor's current drive can be modulated through the encoder to compensate for known cogging torque fluctuations and compensate them using electronic drive techniques. Because the motor configuration already includes a high-resolution encoder, and the equation for cogging torque was also identified in the previous chapter, the subsequent step involves designing control algorithms to effectively compensate for the cogging torque. By implementing these algorithms, the motion accuracy of the motor can be improved, leading to enhanced performance and overall efficiency.

Feedforward control method

Since the cogging torque equation has been derivated, the feedforward control method could be considered as an effective method for compensating the cogging torque. By employing this approach, it becomes possible to predict and counteract the effects of cogging torque, resulting in smoother motor operation and improved performance. Feedforward control allows for precise compensation based on the cogging torque model, thereby enhancing motion accuracy and overall system efficiency.

This feedforward control module operates by taking the reference shoulder position, calculated through inverse kinematics, as its input see Figure 3.5 which extended based on Figure 2.5. Its function is derived from the cogging torque equation identified in the third part of the system. As a result, the feedforward control treats shoulder position variations as disturbances in the system and compensates for them accordingly. This allows it to effectively counteract the influence of cogging torque on the controlled variable.

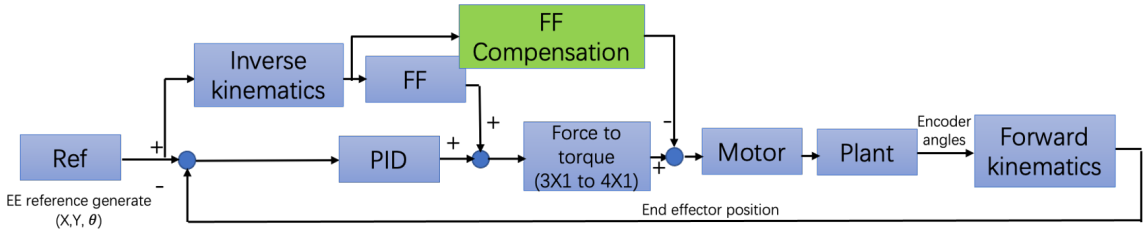

Figure 3.5: Structure of feedforward control

One advantage of this control module is its rapid computation and absence of system delays. Furthermore, it does not require the detection of output variables, only depends on whether the actual motor position, represented by the actual signal, can effectively track the input signal of the feedforward control, which is the reference signal. However, it is essential to acknowledge that the accuracy of the results is dependent on the accuracy of the kinematic model in the redundancy parallel manipulator system. Inaccuracies kinematic models may lead to imprecise outcomes.

Closed-loop feedback compensation control

Using the computed joint angle instead of the actual value may have the advantage in computed time, but it also has a disadvantage because the effectiveness of this approach in a PKM relies on the precision of the inverse kinematics calculation used to determine the shoulder reference position based on the end-effector position. Despite precise calculations, discrepancies may still exist between the calculated values and the actual measurements. To address this, the consideration of using the measured shoulder position as a feedback parameter for compensating cogging torque comes into play. By incorporating actual shoulder position measurements into the control strategy, it becomes possible to improve the overall motion accuracy.

The feedback compensation control method can be treated as establishing a system observer. This observer continuously monitors the actual position of a system, which is typically obtained using encoders. Using the real-time information on the system's position, the observer calculates the cogging torque that is currently affecting the system's behavior. The control system then applies negative feedback, meaning it generates a compensatory control signal to counteract the cogging torque's influence. In essence, the feedback compensation control method acts as a real-time correction mechanism that helps the system operate more smoothly and accurately by actively countering the disruptive effects of cogging torque. A detailed theoretical analysis based on the motor is in Appendix B.

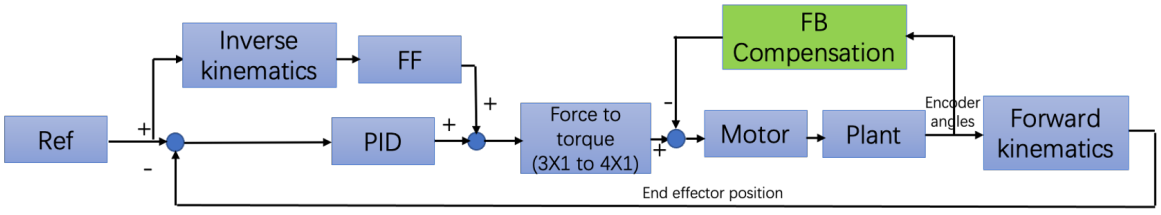

Figure 3.6: Structure of feedback compensation control

Two control algorithms aimed at reducing the cogging effect have been designed. Since practical testing of cogging torque has been conducted in this research, there is no need to explore more complex robust adaptive controllers. Furthermore, the advantage of employing simple control algorithms lies in their ease of implementation and lower hardware requirements in real-world engineering applications. In essence, the principle "simplicity is the ultimate sophistication" holds true, where the simplest control often proves to

be the most optimal. Within the forthcoming subsection, the focus will be directed solely toward presenting the results stemming from tests and simulations involving a single motor with a one-arm configuration.

3.4.2 Single motor simulation

After conducting a thorough analysis and confirming the control method, the system was subjected to simulation analysis based on the chosen control approach. As the data collection and identification were focused on a single motor, the simulation was specifically tailored for this scenario. The single motor model, depicted in the Figure 3.7, was designed with an emphasis on the impact of cogging torque on motion control. However, to simplify the analysis, detailed modeling of the motor, including the current loop, speed loop, and PWM waveform were ingorned.

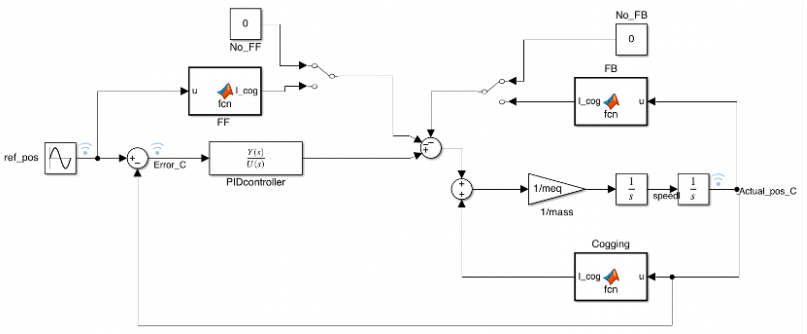

Figure 3.7: One free motor simulink model

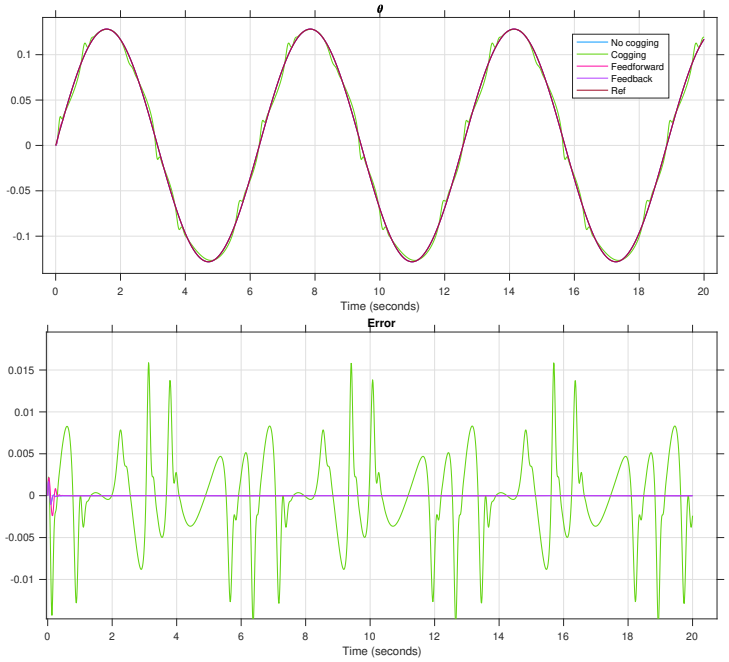

Figure 3.8: One free motor simulation result

The simulation model aims to achieve a sinusoidal target position. By subtracting the actual position from this target, an error signal is obtained. This error signal is transformed into a current input using

PID control, the controller parameter setting is the same with real-time testing model except ω_c. In real-time torque testing, a relatively high crossover frequency $30Hz$ was chosen to minimize the error between the target position and the actual position. However, in simulations, it was observed that the system's bandwidth increased with the utilization of the crossover frequency. When introducing torque ripple in the simulation, the PID controller was already capable of eliminating the cogging effect. Nevertheless, to ensure system stability during actual usage, there are limitations on the crossover frequency. Therefore, in this context, the crossover frequency is set to $15Hz$. Through PID controller, the torque can be calculated, and dividing the m_{eq} results in motor angle acceleration, and after double integration, the motor's orientation is determined. The cogging effect within the model is integrated with the torque input through a cogging function block. To address the cogging effect and facilitate comparison, both feedforward compensation control and feedback compensation control are incorporated into the model. To enhance the comparability between the two control methods, a manual switch is employed.

Two control methods were simulated and evaluated, as illustrated in the Figure 3.8. In the legend, 'Ref' reprensents the motor's reference orientation, 'No cogging' indicates results without cogging effect, 'Cogging' signifies results that do account for the cogging effect, and 'Feedforward' and 'Feedback' denote the simulation result is integration with two cogging reduction control methods. Notably, the simulation model and conditions were somewhat idealized. From the simulation results, it can be observed that without the reduction of cogging effect control, the cogging effect significantly impacts the motor's motion. However, after implementing the reduction cogging effect control method, both control methods exhibit a noticeable reduction in the influence of cogging torque on the target tracking task. Upon closer examination of the amplified results, during the initial phase within the first 0.5 seconds, the feedback observer method has clearly better performance.

It is important to acknowledge that these findings are based on the idealized simulation model, and real-world conditions may present additional challenges. Nevertheless, the results provide promising insights into mitigating cogging torque effects on motion control, offering potential benefits in practical applications.

3.4.3 Single motor test

The data collection platform served as a valuable tool to subject the control methods to practical testing, providing critical insights into their real-world performance. The obtained test results, illustrated in Figure 3.9, offered an evaluation of the control strategies' effectiveness in motion tracking. Figure 3.9(a) shows the tracking performance, Pos_{ref} represents the reference trajectory of the motor, $Pos_{cogging}$ denoted the motor test result which already include cogging effect, Pos_{ff} and Pos_{fb} signify that the test results incorporate feedback and feedforward compensation control methods. Figure 3.9(b) shows the error (Between reference position and measured position) result including the start phase and without start phase, where $err_{cogging}$ is the error without any cogging reduction control, while err_{FB} and err_{FF} is the result including feedback and feed forward mitigation control methods. Without the initial stage overshoot effect, it can more intuitively demonstrate the impact of the control method. From Figure 3.9(b) neither of the methods showed a significant reduction in torque ripple during this experiment. Therefore, we introduce the Root mean square error (RMSE) as an effective metric to demonstrate the performance of various control methods. The result is shown in Table 3.2.

Table 3.2 RMS test error for different setting

Parameter name	Value
With cogging RMSE	0.0015
With FF control RMSE	0.0022
With FB control RMSE	0.0012

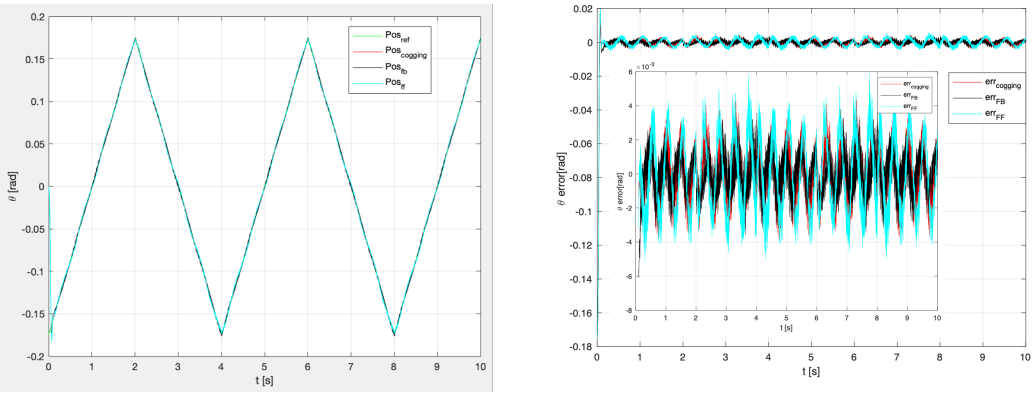

(a) (b)

Figure 3.9: (a)One motor test result (b)Error with and without start phase

One of the control methods tested was the feedforward control. This method utilizes the reference position to pre-calculate and generate a control signal that compensates for the anticipated torque ripple. However, as observed from the test results, it became evident that in the actual system, there were discrepancies between the reference position and the actual position of the motor. These discrepancies resulted in errors in the feedforward control predictions, leading to poor performance of the algorithm in practical applications, to the extent that its performance did not surpass the test results without using the reduction cogging control algorithm.

In contrast, the feedback compensation method demonstrated slightly better performance in the experimental evaluation. Its error signal is smaller than with feedforward control from Figure 3.9 (b) and also has a smaller RMSE value from Table 3.2. This method relies on continuously measuring the motor's actual position and comparing it with the desired reference position. Any deviations or errors between the two positions are used to generate corrective control signals in real-time. This constant feedback loop allows the control system to promptly and accurately adjust the motor's output to achieve the desired motion trajectory. In conclusion, the data-driven practical testing using the data collection platform validated the superiority of the feedback compensation method over the feedforward control in terms of motion tracking performance.

Chapter 4

Results and discussion of simulation and experiments

The simulation and experimental results with cogging reduction control applied to the manipulator will be presented in this chapter. Section 4.1 presents the simulation results, where the cogging effect and cogging reduction models are added to the model based on Chapter 2. The results of the two control algorithms are compared. In practical testing, the encoder measures the motor's relative position, not its absolute position. Section 4.1 also models and simulates this situation to determine its impact on parallel manipulator motion. In Section 4.2, the actual system is tested through a test setup experiment to compare the two control methods.

4.1 SIMULATION RESULT

4.1.1 Simulation result without position offset

Simulation result for tracking performance

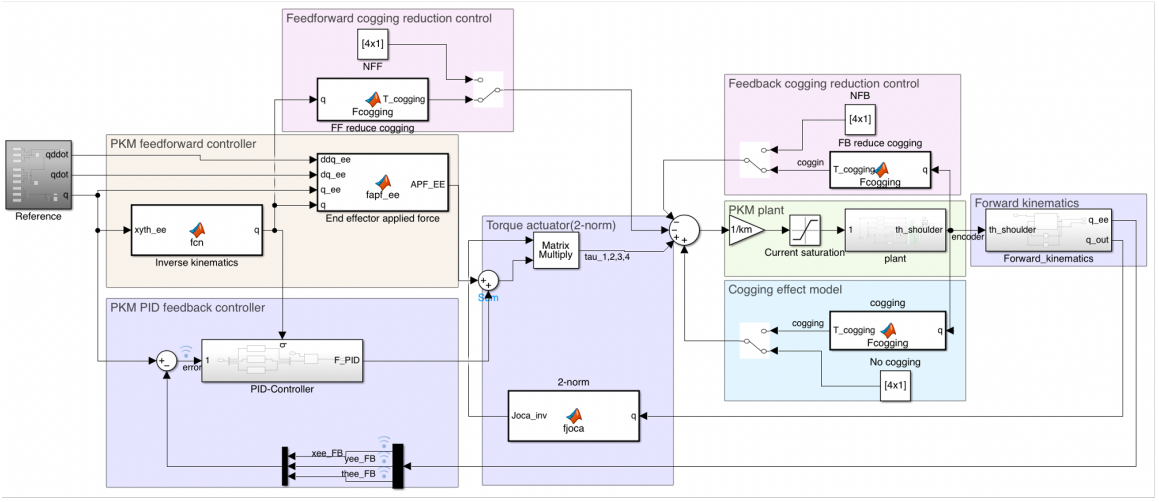

Figure 4.1: Simulation model without position shift

The simulation model of the entire redundant parallel manipulator system has been constructed in Chapter 2. The cogging torque and cogging torque reduction methods have been integrated into the model. The final Simulink block diagram is illustrated in Figure 4.1. In comparison to the dynamic motion model

of the RA-PKM, two additional components have been introduced. The first component involves the incorporation of the cogging torque in the plant model. Initially, the simulations were idealized and did not account for disturbances. Through data acquisition and identification, the equation for torque ripple was derived in section 3.3. This part was added as the cogging torque to the dynamic model of the RA-PKM, which in Figure 4.1 is represented by the cogging effect model block. The second component pertains to the control of the cogging effect. Simulations were conducted for the two control methods mentioned in the previous chapter. Similar with the one-motor simulation model in Chapter 3, two manual switches have been added for the sake of data comparison and simulation convenience. The effectiveness of these methods was compared through the assessment of control outcomes.

In this simulation model, all elements remain consistent with the RA-PKM system's simulation model, except for the inclusion of the cogging torque and its corresponding control section. The PID controller maintains a crossover frequency of $5Hz$, and modules such as feedforward control and torque allocation are identical to those in the RA-PKM model. To compare the torque ripple mitigated control performance, a different reference file has been generated. The simulation results inFigure 4.2 highlight the impact of cogging effect on motion control. The graph illustrates the system's tracking performance and tracking error under various configurations. 'No cogging' signifies that the system operates without considering the cogging effect, and hence also no cogging effect control. 'Cogging' reflects simulation results that incorporate the cogging effect. 'Feedforward' and 'Feedback' represent simulation outcomes with specific control measures applied to mitigate the cogging effect, 'Ref' denotes the reference trajectory.

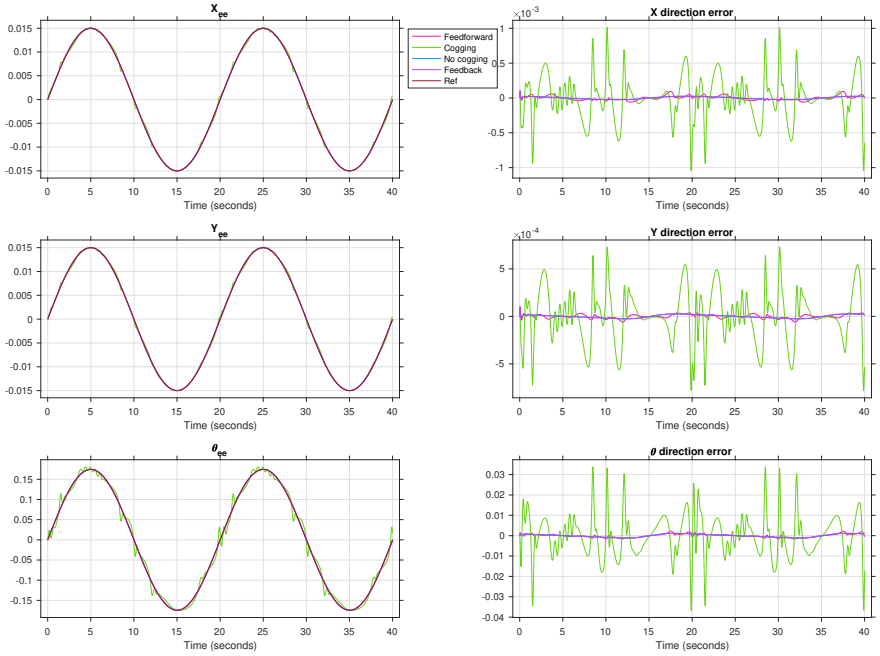

Figure 4.2: Simulation result without position offset

Table 4.1 RMSE for different setting in simulation

Parameter name	$Error_X(m)$	$Error_Y(m)$	$Error_\theta(rad)$
RMSE no cogging	1.187×10^{-5}	9.985×10^{-6}	0.0004328
RMSE with cogging	0.0004314	0.0003669	0.00923
RMSE of with FF control	1.346×10^{-5}	1.19×10^{-5}	0.0004524
RMSE of with FB control	1.187×10^{-5}	9.985×10^{-6}	0.0004328

The simulation result is evident that cogging torque indeed exerts an impact on the system's motion accuracy, particularly pronounced during trajectory tracking in rotations. Notably, after the integration of the cogging torque reduction method, and given the absence of delays and testing errors during the simulation phase, the shoulder reference calculated via inverse kinematics aligns closely with the output from the encoder. Consequently, with the introduction of the cogging torque compensation algorithm, the cogging effect is effectively mitigated, resulting in a motion-tracking performance equivalent to that observed in the absence of cogging disturbances. The RMSE result also shows the same result in Table 4.1, The RMSE with feedback control is the same with no cogging, which means the feedback compensation control eliminates the cogging effect.

The complete RA-PKM system, already includes PKM's PID feedback control and feedforward control based on the Equations of Motion (EOM). Therefore, the setting of the PID controller's crossover frequency also affects the cogging effect. When ω_c is set to $10Hz$, the resulting RMSE is as shown in Table 4.2. Increasing the crossover frequency can enhance the system's tracking performance and, even in the presence of cogging effects, mitigate the impact of cogging torque.

Table 4.2 RMSE for crossover frequency at $10Hz$

Parameter name	$Error_X(m)$	$Error_Y(m)$	$Error_\theta(rad)$
RMSE no cogging	1.481×10^{-6}	1.236×10^{-6}	5.417×10^{-5}
RMSE with cogging	4.08×10^{-5}	3.799×10^{-5}	0.0005653

Simulation result for cogging contribution

In order to better analyze the impact of the cogging effect of each actuator on RA-PKM motion, simulation from each actuator on the motion of the EE has been analyzed to examine the impact of cogging torque on each actuator. Tracking performance can be observed from the Figure 4.3 , where different colors represent different states of motion accuracy. "No cogging" indicates that there is no cogging effect, while cogging from 1, 2, 3, 4 signifies which actuator has cogging torque output. The results reveal that motor2 and motor4 have the most significant impact on translational motion in the X direction, while motor1 and motor3 exhibit a more pronounced effect on the Y direction, with a minimal impact on the X direction. However, it is important to note that all cogging effects will have an influence on the rotational motion in the θ direction.

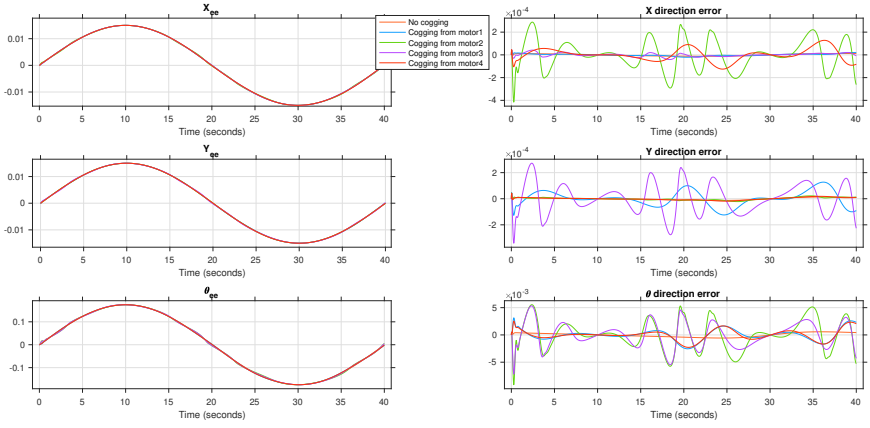

Figure 4.3: Each actuator cogging torque contributes to EE position

4.1.2 Simulation result with position offset

Shoulder initial position offset

An encoder is a type of device that can measure the real-time position of the motor. In this RKM system, the actuator's encoder is an incremental encoder, which means it can sense the relative position of the motor rather than an absolute position. Hence, at the initialization of the dynamic motion of the PKM, the feedback from the encoder may not always provide the utmost precision, thereby introducing the possibility of positional discrepancies. This potential scenario was implemented within the model itself. A positional offset was introduced after the encoder data. Initially, simulations were conducted to assess the impact of this positional offset on motion control. Moreover, a comprehensive examination of the compounded impact of both cogging effects and the initial positional offset. This exploration aims at gauging the responsiveness of the two control algorithms in this context, specifically in their ability to reduce the influence of cogging effects.

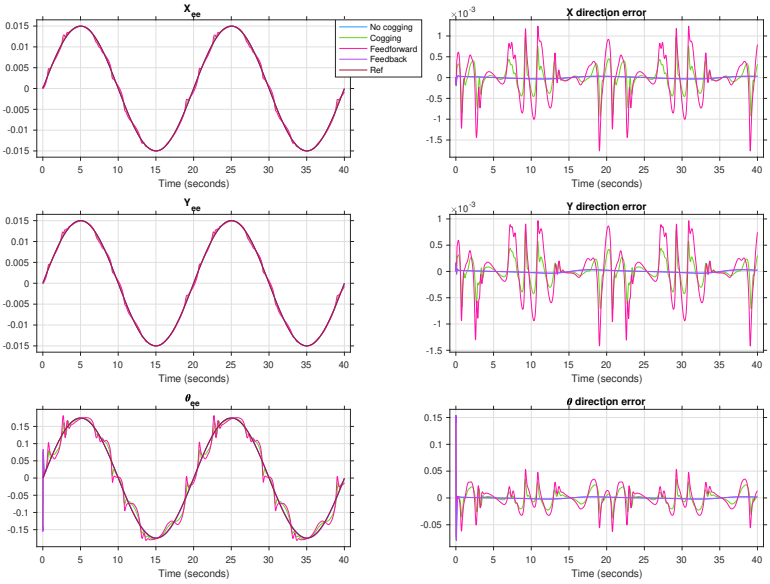

Figure 4.4: Simulation result with initial position offset

Table 4.3 RMSE for different settings with initial offset

Parameter name	$Error_X(m)$	$Error_Y(m)$	$Error_\theta(rad)$
RMSE no cogging	1.511×10^{-5}	1.138×10^{-5}	0.000781
RMSE with cogging	0.0001616	0.0001623	0.0002717
RMSE of with FF control	0.0004388	0.0004308	0.001863
RMSE of with FB control	1.511×10^{-5}	1.138×10^{-5}	0.000781

When there is no influence of cogging effects, the impact of position offset on motion is primarily confined to the initial phase which is shown in Figure 4.4 shows. During this onset, the position response may exhibit an overshoot. After approximately 0.3 seconds, the system effectively tracks the desired target, although the degree of overshoot tends to amplify with an increase in the position shift degree. However, as the overshoot reaches a threshold of 5 degrees, the entire system becomes incapable of handling the situation. Thus, any offset between encoder testing and actual operation should not surpass 5 degrees. Upon the introduction of cogging effects, the initial phase of the position response displays transient overshoot, and its impact on motion accuracy becomes more pronounced compared to scenarios without offsets. Employing both feedforward and feedback compensation techniques to mitigate the influence of cogging

torque on motion, we observed that due to the presence of position offsets, feedforward compensation cannot precisely counteract cogging torque. Consequently, its effect on enhancing motion accuracy is nearly negligible. On the other hand, the performance of feedback compensation proves to be superior. RMSEresults shown inTable 4.3 also indicate that feedback compensation control completely eliminates the cogging effect. Through this control algorithm, tracking performance aligns seamlessly with scenarios devoid of cogging effects. Hence, the presence of position offsets solely affects the initial phase. Moreover, even in the presence of cogging effects, as long as the compensation is adequately precise, feedback control compensation can effectively alleviate the influence of cogging effects on motion accuracy.

Encoder position offset

Since the encoder counts start from 0 degrees each time the system is powered on. The compensation equation for cogging torque is derived from practical experiments and identification, with the initial rotor position of the motor starting from 0 as well. While using precise feedback compensation for individual motors can reduce cogging effects, the redundancy parallel manipulator system in question has four actuators. Due to its compliant mechanism characteristics, interactions involving potential energy in the robotic arm can result in deviations in the initial motor positions. This means that the encoder-measured motor zero position does not correspond to the actual motor zero position. The purpose of this simulation is to model the effect of the feedback compensation control algorithm when discrepancies exist between encoder measurements and actual positions.

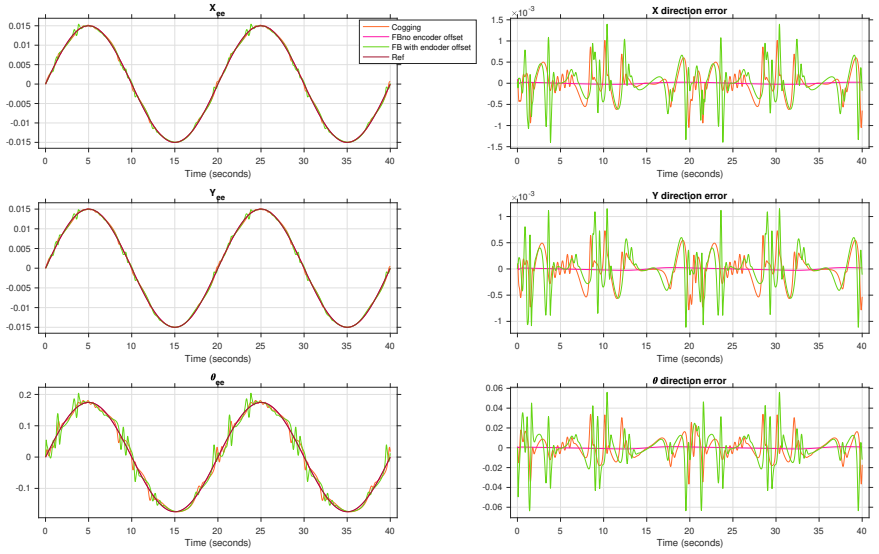

Figure 4.5: Simulation result with encoder offset

Table 4.4 RMSE for different settings with encoder offset

Parameter name	$Error_X(m)$	$Error_Y(m)$	$Error_\theta(rad)$
RMSE no cogging	1.187×10^{-5}	9.985×10^{-6}	0.0004328
RMSE with cogging	0.0004314	0.0003669	0.00923
RMSE of with FF control	1.346×10^{-5}	1.19×10^{-5}	0.0004524
RMSE of with FB control	0.0005476	0.0003411	0.0186

In this simulation model, the real cogging torque integrates encoder values into the dynamic model as input. The feedback compensation model takes into account the potential differences between the real encoder values and the tested data and uses encoder values offset by $1deg$ as input to the compensation model. The simulation results are shown in Figure 4.5, RMSE results shown in Table 4.4. The model that employed

feedback compensation control achieved the poorest system tracking performance. As can also be seen in Figure 4.6, there is a noticeable difference between the compensatory torque and the actual torque. Introducing a $1deg$ offset as input resulted in a significant disparity between the estimated cogging torque and the real torque. The analysis of the simulation results provides clear insights into the impact of positional offsets present in the encoder measurements on the performance of the feedback compensation control strategy aimed at alleviating the cogging effect. These findings highlight the significant role that accurate encoder measurements play in the effectiveness of such compensation approaches. At certain positions within the system's operational range, the interaction between the applied compensation and the inherent cogging effect amplifies motion irregularities. This phenomenon results in a situation where, instead of improving motion accuracy, the feedback compensation control can inadvertently exacerbate deviations in the system's trajectory, consequently leading to decreased overall accuracy. While the intention behind feedback compensation is to counteract the undesirable cogging effect, the simulation outcomes reveal that this endeavor can be impeded by the unavoidable inaccuracies in encoder measurements.

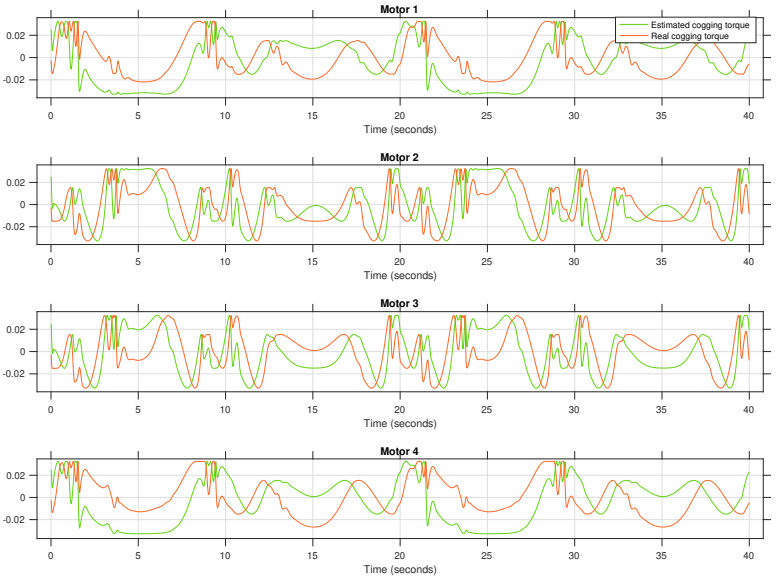

Figure 4.6: Comparison of estimated cogging torque and real cogging torque

4.2 EXPERIMENT TEST RESULTS AND DISCUSSION

The real-time testing model and setup closely mirror the simulation model detailed in Section 4.1.1, with the exception of the plant model component and stop simulation block, as illustrated in the Figure 4.7. The plant model represents the complete real RA-PKM system, so the test includes various intricate factors, such as the interplay of multiple kinematic chains, actuator dynamics, and system complexities. While the stop simulation block takes into account the physical limits of the shoulder joints and EE position. In this configuration, both the PID controller and feedforward controller compute the applied force to the end-effector (EE) based on factors like position error and reference position. The torque allocation module calculates the necessary torque using a 2-norm approach, which is then converted into current requirements using the torque constant. These current requirements are subsequently transformed into analog signals via the NI PCI-6221 DAC module. These analog signals are the inputs into the four actuators according to the real connection. Meanwhile, the encoder measures the actual motor angle, serving as an input for forward kinematics calculations to derive the EE's position, thus providing critical feedback for the system.

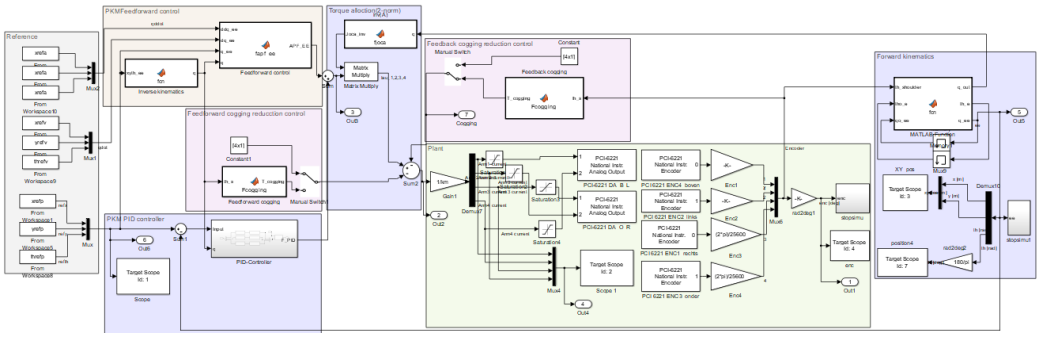

Figure 4.7: Real-time test model

The experimental results are shown in Figure 4.8. It displays the trajectory performance and error outcomes in the 3-DOF dimensions, specifically in the x, y, and θ directions. The subscript label 'ref' signifies the reference tracking trajectory, 'cog' denotes the test results conducted without the implementation of cogging reduction control, while 'FF' and 'FB' correspond to the results achieved through the utilization of feedforward and feedback cogging reduction methods, respectively.

From the test result, the RA-PKM system aligns with concerns previously identified in simulations. From the RMSE of the complete manipulator test in x,y and θ direction which shows in Table 4.5 also verify this result. The algorithm relying on actual encoder positions for feedback compensation control exhibits the poorest performance due to intricate interactions among the 4-link chains and actuators. This inferior performance stems from the inherent discrepancies between the tested encoder positions and the precise motor positions, consequently impairing motion accuracy. Both feedforward and feedback control methods exhibit reduced effectiveness compared to the baseline system without any control algorithm. Of the two reduction control methods, feedforward control displays a better performance. Regrettably, the introduction of the cogging reduction control module fails to enhance the system's motion accuracy. Paradoxically, this module's imprecise compensation introduces perturbations that, in turn, diminish tracking performance.

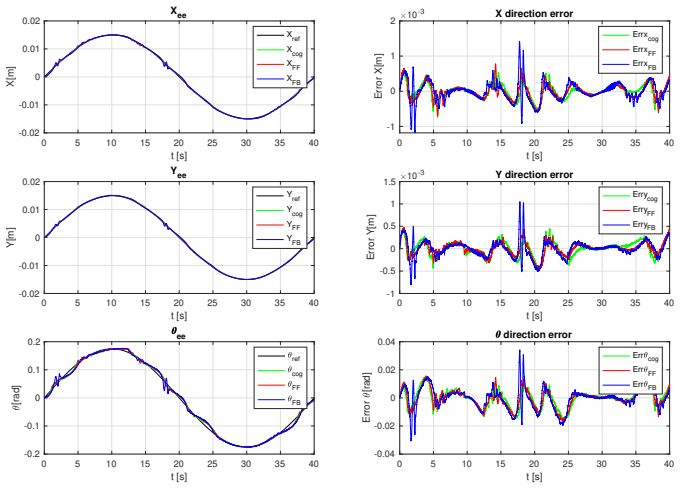

Figure 4.8: Experiment test result comparison

Table 4.5 RMSE for complete manipulator ($\omega_c = 5Hz$)

Parameter name	$Error_X(m)$	$Error_Y(m)$	$Error_\theta(rad)$
RMSE of no cogging reduction control	0.00021	0.00016	0.0068
RMSE of with FF control	0.00024	0.00015	0.0076
RMSE of with FB control	0.00027	0.00019	0.0081

From the comparison of results with and without feedback and feedforward cogging compensation control, as shown in Figure 4.9, 'No cogging' represents the results without cogging effects, 'With cogging' includes the influence of cogging effects, 'Feedforward control' incorporates feedforward cogging compensation control, and 'Feedback control' incorporates feedback cogging compensation control.

It can be observed that in Figure 4.9 (a) which shows the simulation results, due to the precise compensation equation, the cogging effect can be effectively reduced. This allows the RA-PKM's original control output to be in perfect alignment with that of a system without cogging effect. The PID control of the original RA-PKM system may not require adjustment to account for motion inaccuracies caused by the cogging effect. However, in Figure 4.9 (b), the test results show that the cogging reduction compensation has a minimal impact, and in some cases, due to inaccurate compensation, PID control intervention is needed to adjust for errors caused by both the cogging effect and compensation inaccuracies.

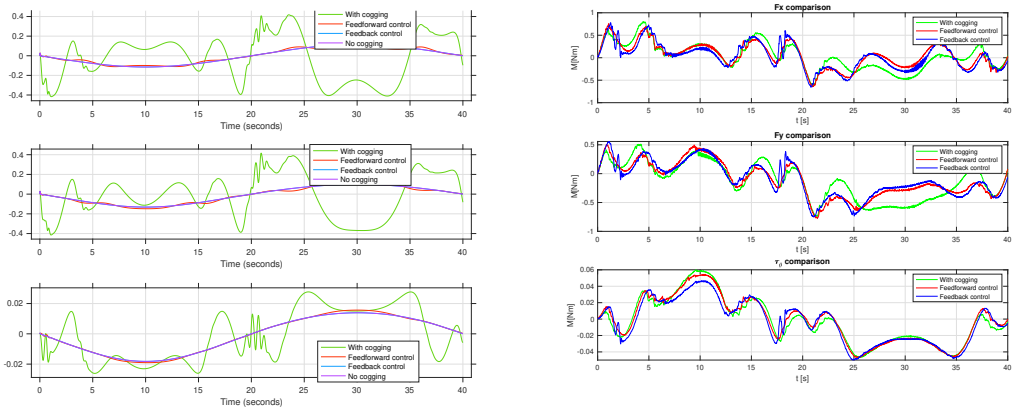

(a) (b)

Figure 4.9: (a)Simulation comparison RA-PKM control of EE applied force (b)Test comparison test RA-PKM control of EE applied force

From the analysis above, it is evident that feedforward and feedback compensation have an impact on the control output of the PKM system. Similarly, the PID controller also affects feedforward and feedback compensation control. During simulation, when the PID controller's crossover frequency is set at $10Hz$, the RA-PKM controller can effectively handle the effects of cogging torque. However, in real-time testing, setting the crossover frequency to the same value not only fails to address the impact of cogging torque but also introduces more noise due to the higher bandwidth, causing system instability and strong oscillations. Therefore, we attempted to reduce the crossover frequency to $3Hz$, as shown in Figure 4.10, With the lowered system bandwidth, tracking performance weakened, making it challenging to closely follow the reference trajectory. The cogging effect became more pronounced, as evidenced by the RMSE analysis in Table 4.6. In the θ direction, the effects of feedforward and feedback compensation control have better performance at rotation direction, but due to compensation inaccuracies, their performance improvements are not significant, and it is particularly evident that feedback control performs exceptionally well in the positive direction wit time range from $0s$ to $20s$, with tracking results consistently better than those without

cogging torque reduction control. However, in the negative direction with a time range from $20s$ to $40s$, the opposite performance is observed. This may be due to changes in the EE reference direction, resulting in varying rotations of the four motors. Because all motors use the same compensation cogging equation, it is possible that some motors have inaccurate compensation equations, leading to this issue.

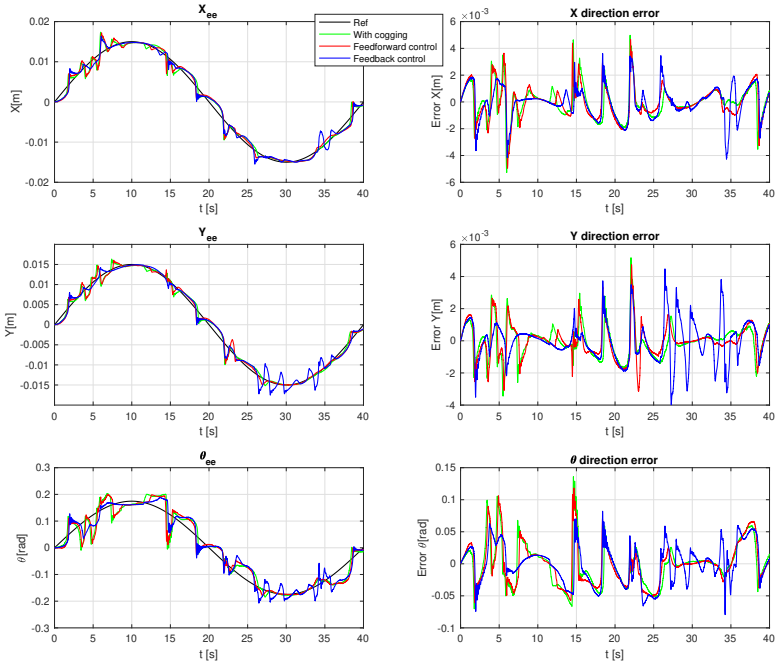

Figure 4.10: Tracking performance when crossover frequency setting is 3Hz

Table 4.6 RMSE for complete manipulator ($\omega_c = 3Hz$)

Parameter name	$Error_X(m)$	$Error_Y(m)$	$Error_\theta(rad)$
RMSE of no cogging reduction control	0.0012	0.001	0.0335
RMSE of with FF control	0.0012	0.001	0.0325
RMSE of with FB control	0.0012	0.0012	0.0302

For RA-PKM system, the cogging effect arises from the interactions among the four actuators. In order to reduce cogging effects, it is necessary to accurately measure or identify the cogging torque of each motor. Especially when the original feedback PID controller has already attenuated the disturbances caused by cogging torque, precise compensation becomes even more important. Therefore, the main reasons why reducing cogging torque control is not effective are as follows:

Firstly, the cogging torque is evaluated for one motor independently and the compensation method applied the same equation for each motor, but it is not how it will work out in reality. Figure 4.11 shows the fitting result for a different motor, red line represents motor1 cogging torque, and blue line is motor2 cogging torque. Although the periods and amplitudes of the cogging torques of both motors are the same, there is an offset in their positions. As a result, the cogging torques for each motor may differ. Additionally, there may be disparities between the results obtained from identifying the free motor and those from the RA-PKM system. In the case of the free motor, the test results involve determining the motor's position and torque when it is in the position of minimum energy. However, for the RA-PKM system, due to the

presence of redundancy, the calculation of torque allocation is based on minimizing the energy of the entire system's end-effector tracking. This fundamental difference can lead to variations in the research project results. The cogging torque equation is directly obtained from testing data using an existing experimental setup. While the results from testing a single motor (one arm) were used to validate the testing method, there are significant differences between the complete system and one arm system. Furthermore, after the completion of the complete system assembly, there were differences between the cogging fitting obtained from testing one of the free motors and the previous fitting results. Therefore, using the method of torque collection from one free motor powered on, the torque ripple contains too many interfering factors, which may result in less accurate measurement of the cogging torque. This, in turn, leads to an inability to correctly compensate for the cogging effect.

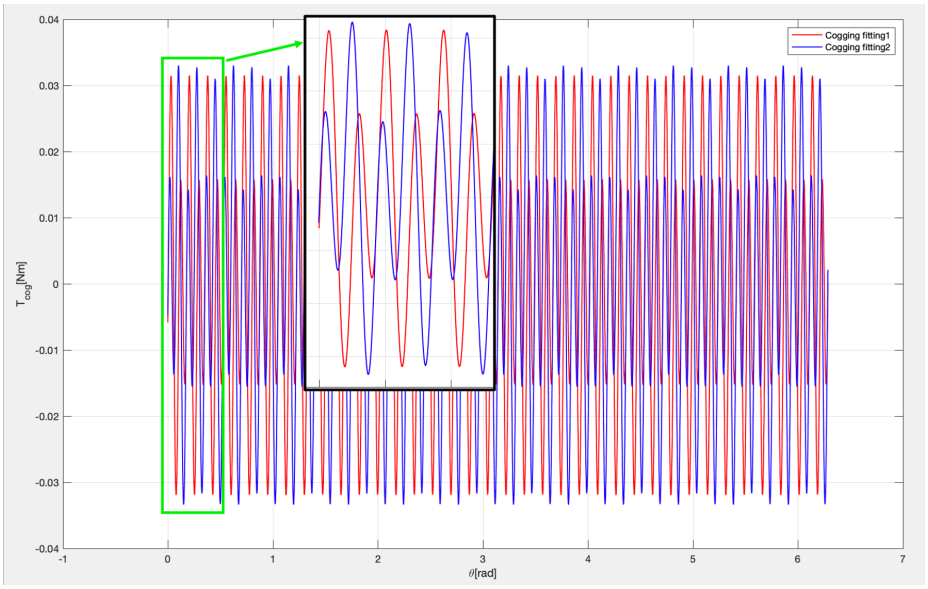

Figure 4.11: Cogging fitting for different motors

Secondly, distinct operating conditions, unlike the conditions experienced by a single motor, the RA-PKM motor's rotation is interdependent. Consequently, compensation equations designed for individual motors prove ineffective in this scenario, which may because the encoder offset was mentioned in prior simulations. Due to the influence of various link chains and compliant mechanisms, there exists a slight deviation between the encoder's measurement position and the actual position of the motor. This disparity prevents the system from achieving accurate compensation. So a new approach is needed which involves the reevaluation of cogging torque for each motor within the complete system.

In summary, mitigating the influence of cogging torque necessitates the precise determination of motor positions and the correct formulation of the cogging torque equation for comprehensive system compensation.

Chapter 5

Conclusion and future directions

5.1 CONCLUSION

The purpose of this study is to identify the equation for cogging torque through testing methods, and design methods to improve the motion accuracy of the RA-PKM by compensating for cogging torque. In the end, the feasibility of the algorithm was verified through simulation. Due to the complexity of the actual system, cogging torque compensation in the actual complete system could not accurately and precisely compensate for the discrepancy in real time, so the actual testing did not achieve the expected results.

In this thesis, the EOM for the RA-PKM has been derived, and a corresponding simulation model has been established. The collection of cogging torque data was based on an existing platform, and we utilized the parameter identification method to derive the cogging equation. To mitigate the adverse effects of cogging on the system's motion, the feedback and feedforward compensation control methods were derived. The feasibility of these approaches has been assessed through simulations and experiments. In consideration of real-world challenges, simulations for two distinct scenarios: one involving initial shoulder position offsets and the other dealing with encoder position offsets were conducted.

While the practical experiments did not quite meet the goal of improving motion accuracy, simulation-based analysis yielded insights. Specifically, we were able to quantify how the cogging effects of the four motors influence the position of the EE.

Overall, this study has examined cogging torque and its impact on the motion accuracy of the RA-PKM system, providing insights into both theoretical derivations and practical applications. It has illuminated the complexities involved in mitigating cogging effects to enhance motion precision.

5.2 FUTURE DIRECTIONS

In this research, simulations indicate that both feedback and feedforward control can reduce the cogging effect. However, experiments did not yield the same conclusion. Therefore, future work should focus on how to obtain an accurate cogging compensation equation and correct motor position to enable more precise cogging effect compensation in practical applications.

Because the source of the cogging effect is the actuators, in order to improve the motion accuracy of RA-PKM by reducing the cogging effect, it is necessary, as mentioned in this thesis, to compensate for individual motors. In future work, there is a need to test four motors' cogging equations and validate the accuracy of this equation, possibly through a combination of FEM and analytical methods. Through comparing experimental identification results with analytical findings to ascertain the precision of the identification cogging equation.

Another aspect to address the problem is resolving the encoder offset issue. Firstly, after assembly of the RA-PKM system, identifying the system's zero position is crucial, which includes implementing the

homing procedure for the system. This procedure ensures that the motor starts in the same position every time. Determining this starting position allows for compensation control using the correct cogging equation. It can also be achieved by calibrating the zero points of each motor every time the controller is started, ensuring that the motors start at their zero positions to guarantee the accuracy of encoder measurements. Finally, this can be accomplished by replacing the encoder to convert the measured relative angle into an absolute angle, which can avoid the zeroing and homing procedure. To enable the use of the cogging equation identified for a single motor, it should be ensured that the absolute angles during the identification of that isolated motor are identical to the absolute angles in the assembled set-up. Absolute encoders may offer this capability. Homing or zero calibration only guarantees this if the motors can be identified separately without removing them from the set-up, for example, by decoupling the upper arm at its elbow joint from the rest of the manipulator.

The RA-PKM system is a high-precision system, and the cogging equation obtained through fitting may have some deviation from reality. Adaptive control methods, such as adding observers to the motor's inner-loop control to estimate the motor's position and cogging torque, can be employed. Through real-time updates, cogging torque can be compensated for more accurately. This method requires hardware with high computational capabilities.

List of References

[1] J.-P. Merlet, *Parallel robots*. Springer Science & Business Media, 2006, vol. 128.

[2] W. Shang, S. Cong, and Y. Ge, "Coordination motion control in the task space for parallel manipulators with actuation redundancy," *IEEE Transactions on Automation Science and Engineering*, vol. 10, no. 3, pp. 665–673, 2012.

[3] A. Müller, *Redundant actuation of parallel manipulators*. INTECH Open Access Publisher, 2008.

[4] J. A. G. Sanchez, *Statically Balanced Compliant Mechanisms: Theory and Synthesis*. Technische Universtiteit Delft, 2013.

[5] L. L. Howell, "Introduction to compliant mechanisms," *Handbook of Compliant Mechanisms*, pp. 1–13, 2013.

[6] J.B.Jonker, R.G.K.M.Aarts, and J. Meijaard, *Flexible multibody dynamics for design purposes-A Finite Element Approach*. Universiteit Twente,Enschede, SEP.2020.

[7] P. Stoffels, "Optimization and control of a redundantly actuated 3-DOF planar manipulator with flexure joints," M.S. thesis, University of twente, 2021.

[8] D. Berendsen, "2-DOF planar redundantly actuated parallel kinematic manipulator with flexure joints optimization and control," M.S. thesis, University of twente, 2021.

[9] Renesas, *What are brushless DC motors*. [Online]. Available: `https://www.renesas.cn/cn/en/support/engineer-school/brushless-dc-motor-02-inverter-pmw`.

[10] D. Chowdhury, M. Chattopadhyay, and P. Roy, "Modelling and simulation of cost-effective sensorless drive for brushless dc motor," *Procedia Technology*, vol. 10, pp. 279–286, 2013.

[11] M. Thiele, *Analysis of cogging torque due to manufacturing variations in fractional pitch permanent magnet synchronous machines*. Charles Darwin University (Australia), 2013.

[12] Y.-X. Zhang, S. Cong, W.-W. Shang, Z.-X. Li, and S.-L. Jiang, "Modeling, identification and control of a redundant planar 2-dof parallel manipulator," *International Journal of Control Automation and Systems*, vol. 5, no. 5, pp. 559–569, 2007.

[13] H. Cheng, Y.-K. Yiu, and Z. Li, "Dynamics and control of redundantly actuated parallel manipulators," *IEEE/ASME Transactions on mechatronics*, vol. 8, no. 4, pp. 483–491, 2003.

[14] K. Krajoski, A. Müller, H. Gattringer, and M. Jörgl, "Design, modeling and control of an experimental redundantly actuated parallel platform," in *Proceedings of the OAGM&ARW Joint Workshop*, 2016, pp. 209–216.

[15] C. Gosselin and L.-T. Schreiber, "Redundancy in parallel mechanisms: A review," *Applied Mechanics Reviews*, vol. 70, no. 1, p. 010 802, 2018.

[16] M. Aydin, "Magnet skew in cogging torque minimization of axial gap permanent magnet motors," in *2008 18th International Conference on Electrical Machines*, IEEE, 2008, pp. 1–6.

[17] G. Otten, T. J. De Vries, J. Van Amerongen, A. M. Rankers, and E. W. Gaal, "Linear motor motion control using a learning feedforward controller," *IEEE/ASME transactions on mechatronics*, vol. 2, no. 3, pp. 179–187, 1997.

[18] L. Xu and B. Yao, "Adaptive robust precision motion control of linear motors with ripple force compensations: Theory and experiments," in *Proceedings of the 2000. IEEE International Conference on Control Applications. Conference Proceedings (Cat. No. 00CH37162)*, IEEE, 2000, pp. 373–378.

[19] C. Röhrig and A. Jochheim, "Motion control of linear synchronous motors with force ripple compensation using current shaping," *IFAC Proceedings Volumes*, vol. 35, no. 1, pp. 85–90, 2002.

[20] B. Grcar, P. Cafuta, G. Stumberger, and A. M. Stankovic, "Control-based reduction of pulsating torque for pmac machines," *IEEE Transactions on Energy Conversion*, vol. 17, no. 2, pp. 169–175, 2002.

[21] P. Dini and S. Saponara, "Design of an observer-based architecture and non-linear control algorithm for cogging torque reduction in synchronous motors," *Energies*, vol. 13, no. 8, p. 2077, 2020.

[22] Z. Ning, L. Ling, L. Dan, and Y. Shuping, "Measuring cogging torque in permanent magnet electric machines," *Micromotors*, vol. 45, no. 10, pp. 23–27, 2012.

[23] K. Lee, J. Kim, and Y. Lee, "A simple method of measuring cogging torque in bldc motors using dynamometer," in *2018 IEEE International Conference on Consumer Electronics-Asia (ICCE-Asia)*, IEEE, 2018, pp. 206–212.

[24] Z. Zhu, "A simple method for measuring cogging torque in permanent magnet machines," in *2009 IEEE Power & Energy Society General Meeting*, IEEE, 2009, pp. 1–4.

[25] L. Dong, *Research on Design, Multibody Dynamics and Control of Redundant Parallel Robot with Multiple Actuation Modes*. Tianjin University (China), 2017.

[26] J. Van Dijk and R. Aarts, "Analytical one parameter method for PID motion controller settings," *IFAC Proceedings Volumes*, vol. 45, no. 3, pp. 223–228, 2012.

[27] R. Aarts and G. Romer, *Design and control of mechatronic systems*. University of twente, 2022.

[28] W. Xiuhe, *Permanent magnet motor*. China Electric Power Press, 2010.

[29] Y. Wang, J. Shen, Z. Fang, and W. Fei, "Reduction of cogging torque in permanent magnet flux-switching machines," *Journal of Electromagnetic Analysis and Applications*, vol. 2009, 2009.

[30] T. Tudorache, I. Trifu, C. Ghita, and V. Bostan, "Improved mathematical model of pmsm taking into account cogging torque oscillations," *Advances in Electrical and Computer Engineering*, vol. 12, no. 3, pp. 59–64, 2012.

[31] N. Bianchi and S. Bolognani, "Design techniques for reducing the cogging torque in surface-mounted pm motors," *IEEE Transactions on industry applications*, vol. 38, no. 5, pp. 1259–1265, 2002.

[32] M. Wang, L. Li, D. Pan, Y. Tang, and Q. Guo, "High-bandwidth and strong robust current regulation for pmlsm drives considering thrust ripple," *IEEE Transactions on Power Electronics*, vol. 31, no. 9, pp. 6646–6657, 2015.

Appendix A

Constraint equation

The geometric constraint equation for the RA-PKM redundancy manipulator system is:

$$H(q) = \begin{bmatrix} x_{1com1} - x_A - L_{1com}\cos(\theta_{1s}) \\ y_{1com1} - y_A - L_{1com}\sin(\theta_{1s}) \\ x_{1com2} - x_A - L_1\cos(\theta_{1s}) - L_{2com}\cos(\theta_{1s}+\theta_{1e}) \\ y_{1com2} - y_A - L_1\sin(\theta_{1s}) - L_{2com}\sin(\theta_{1s}+\theta_{1e}) \\ x_{2com1} - x_D - L_{1com}\cos(\theta_{2s}) \\ y_{2com1} - y_D - L_{1com}\sin(\theta_{2s}) \\ x_{2com2} - x_D - L_1\cos(\theta_{2s}) - L_{2com}\cos(\theta_{2s}+\theta_{2e}) \\ y_{2com2} - y_D - L_1\sin(\theta_{2s}) - L_{2com}\sin(\theta_{2s}+\theta_{2e}) \\ x_{3com1} - x_G - L_{1com}\cos(\theta_{3s}) \\ y_{3com1} - y_G - L_{1com}\sin(\theta_{3s}) \\ x_{3com2} - x_G - L_1\cos(\theta_{3s}) - L_{com}\cos(\theta_{3s}+\theta_{3e}) \\ y_{3com2} - y_G - L_1\sin(\theta_{3s}) - L_{2com}\sin(\theta_{3s}+\theta_{3e}) \\ x_{4com1} - x_J - L_{1com}\cos(\theta_{4s}) \\ y_{4com1} - y_J - L_{1com}\sin(\theta_{4s}) \\ x_{4com2} - x_J - L_1\cos(\theta_{4s}) - L_{2com}\cos(\theta_{4s}+\theta_{4e}) \\ y_{4com2} - y_J - L_1\sin(\theta_{4s}) - L_{2com}\sin(\theta_{4s}+\theta_{4e}) \\ x_A + L_1\cos(\theta_{1s}) + L_2\cos(\theta_{1s}+\theta_{1e}) - \frac{\sqrt{2}}{2}L_3\cos(\theta_{ee}+\frac{3}{4}\pi) - x_{ee} \\ y_A + L_1\sin(\theta_{1s}) + L_2\sin(\theta_{1s}+\theta_{1e}) - \frac{\sqrt{2}}{2}L_3\sin(\theta_{ee}+\frac{3}{4}\pi) - y_{ee} \\ x_D + L_1\cos(\theta_{2s}) + L_2\cos(\theta_{2s}+\theta_{2e}) - \frac{\sqrt{2}}{2}L_3\cos(\theta_{ee}-\frac{3}{4}\pi) - x_{ee} \\ y_D + L_1\sin(\theta_{2s}) + L_2\sin(\theta_{2s}+\theta_{2e}) - \frac{\sqrt{2}}{2}L_3\sin(\theta_{ee}-\frac{3}{4}\pi) - y_{ee} \\ x_G + L_1\cos(\theta_{3s}) + L_2\cos(\theta_{3s}+\theta_{3e}) - \frac{\sqrt{2}}{2}L_3\cos(\theta_{ee}-\frac{1}{4}\pi) - x_{ee} \\ y_G + L_1\sin(\theta_{3s}) + L_2\sin(\theta_{3s}+\theta_{3e}) - \frac{\sqrt{2}}{2}L_3\sin(\theta_{ee}-\frac{1}{4}\pi) - y_{ee} \\ x_J + L_1\cos(\theta_{4s}) + L_2\cos(\theta_{4s}+\theta_{4e}) - \frac{\sqrt{2}}{2}L_3\cos(\theta_{ee}+\frac{1}{4}\pi) - x_{ee} \\ y_J + L_1\sin(\theta_{4s}) + L_2\sin(\theta_{4s}+\theta_{4e}) - \frac{\sqrt{2}}{2}L_3\sin(\theta_{ee}+\frac{1}{4}\pi) - y_{ee} \end{bmatrix} = 0 \qquad \text{(A.1)}$$

Where L_{1com} is the length from the shoulder joint to upper arm central of mass.L_{2com} is the length of the elbow joint to the lower arm central of mass.

Appendix B

Feedback compensation control theory analysis

To analyze the feasibility of feedback compensation in a motor, the speed closed-loop control principle of the motor is shown in the Figure B.1. The reason for employing a speed closed-loop control circuit is to enable the analysis of motor stability using a second-order system. Through the analysis of the motor circuit, the feasibility of this compensation method can be explained. In the block diagram, Ref represents the reference value of the motor speed, ε denotes the error between the measured and target values, C represents the controller, and I(can also be U) stands for the input current (voltage) to the motor. P represents the motor model, and Y is the motor's output speed. Typically, the controller may have an inner current control loop, allowing the current to serve as the output of the controller. Assuming the motor follows an ideal model, the thrust output is directly proportional to the current. Thus, the transfer function can be represented as (B.1):

Figure B.1: Block diagram motor control system

$$Y(s) = \frac{K_m}{ms} I(s) \tag{B.1}$$

In the equation, m denotes the mass, K_m is the torque constant, it is a constant value, normally, the motor current control uses PI controller, so the transfer function for the controller is (B.2):

$$I(s) = (K_p + \frac{K_i}{s})\varepsilon(s) \tag{B.2}$$

K_p and K_i are the proportional and integral factors of the control system, respectively. The transfer function of the entire system from reference speed to actual speed is given by (B.3).

$$Y(s) = \frac{K_m K_p s + K_m K_i}{ms^2 + K_m K_p s + K_m k_i} R(s) \tag{B.3}$$

From this equation, it is evident that the system is a typical second-order system since, in general, $K_p > K_i$. Therefore, the damping factor of this system is greater than 1, resulting in a step response without overshoot. However, in reality, due to the presence of cogging force, the motor's transfer function needs to be modified.

$$Y(s) = \frac{K_m I(s) + T_c[\frac{Y(s)}{s}]}{ms} \tag{B.4}$$

T_c represents the cogging torque formula of the motor, which varies periodically with the motor's position. Since T_c has already been identified, so by linearizing T_c around any equilibrium point and setting this point

as the initial position, the above equation can be simplified as follows:

$$Y(s) = \frac{K_m s}{ms^2 - K_{cg}} I(s) \tag{B.5}$$

The new transfer function for the motor is :

$$Y(s) = \frac{K_m K_p s + K_m K_i}{ms^2 + K_m K_p s + K_m k_i - K_{cg}} R(s) \tag{B.6}$$

The corrected system remains a second-order system, but due to the influence of cogging torque, the system may exhibit damping oscillations. If K_{cg} is significantly large, the system might even become unstable. To address this, position closed-loop feedback is introduced, and its block diagram is shown in the Figure B.2.

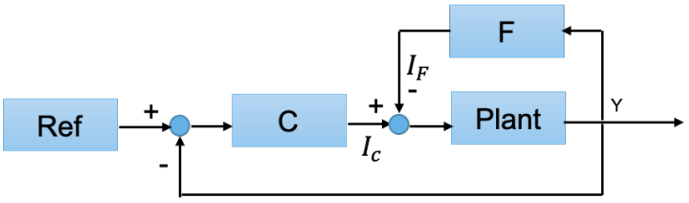

Figure B.2: Motor with position feedback cogging compensation

In the figure, I_c represents the output of the PID controller, while I_F corresponds to the newly added position feedback loop (where the position signal is obtained by integrating Y). The output I_F is used to compensate for the cogging effect in the motor. The transfer function of I_F is given by:

$$I_F(s) = \frac{K_{cg}}{K_m s} Y(s) \tag{B.7}$$

Based on the structure shown in Figure B.2, the final transfer function can be calculated, and it becomes identical to that of the system without cogging torque. In other words, this structure eliminates the influence caused by T_c. Introducing position feedback is equivalent to establishing a model of cogging force within the control system, and it compensates for the actual cogging force through negative feedback.